Journal of Physics D: Applied Physics

PAPER • **OPEN ACCESS**

Magnetic enhancement of the electrical asymmetry effect in capacitively coupled plasmas

To cite this article: Scott J Doyle *et al* 2024 *J. Phys. D: Appl. Phys.* **57** 315204

OPEN ACCESS
IOP Publishing
Journal of Physics D: Applied Physics
J. Phys. D: Appl. Phys. **57** (2024) 315204 (20pp)
https://doi.org/10.1088/1361-6463/ad3f26

Magnetic enhancement of the electrical asymmetry effect in capacitively coupled plasmas

Scott J Doyle[1,3,*], Rod W Boswell[2], Christine Charles[2] and James P Dedrick[3]

[1] Department of Physics, School of Natural & Computing Sciences, University of Aberdeen, King's College, Aberdeen AB24 3FX, United Kingdom
[2] Space Plasma, Power and Propulsion Laboratory, Research School of Physics and Engineering, The Australian National University, Canberra ACT 2601, Australia
[3] York Plasma Institute, School of Physics, Engineering and Technology, University of York, Heslington, York YO10 5DD, United Kingdom

E-mail: Scott.Doyle@Physics.org

Received 16 October 2023, revised 27 February 2024
Accepted for publication 16 April 2024
Published 9 May 2024

Abstract

The development of real-time control strategies for key discharge parameters, such as densities, fluxes, and energy distributions, is of fundamental interest to many plasma sources. Over the last decade, multi-harmonic 'tailored' voltage waveforms have been successfully employed to achieve enhanced control of key parameters in a wide range of radio-frequency (RF) plasma sources through application of the electrical asymmetry effect (EAE). More recently, the analogous magnetic asymmetry effect (MAE) has been numerically and experimentally demonstrated to achieve a notable degree of control in parallel plate RF plasma sources. The MAE is achieved via selectively magnetising the charged species adjacent to one electrode, altering the charge flux to the surface and enforcing a DC self-bias to maintain quasineutrality. This study addresses the degree of control achieved by the MAE in a non-planar geometry via 2D fluid/kinetic simulations of a magnetised RF capacitively coupled plasma source employing two different magnetic topologies. The simultaneous application of the EAE and MAE is then presented for the same geometry, demonstrating a degree of non-linear behaviour dependant upon the applied magnetic topology. Control of the DC self-bias voltage η_{dc} is demonstrated for a single 600 V_{pp}, 13.56 MHz discharge in both 'convergent' (maximum on-axis field strength) and 'divergent' (minimum on-axis field strength) magnetic topolgies. MAE induced modulations of $\eta_{dc} = 0.13\ V_{pp}$ and $\eta_{dc} = 0.03\ V_{pp}$ are achieved for each magnetic topology, respectively, for magnetic field strengths between 50 and 1000 G. Simultaneous application of an EAE and MAE is achieved through a multi-harmonic 'peak'-type tailored voltage waveform employing varying harmonic phase offsets between $0° \leqslant \theta \leqslant 360°$. The degree to which the DC self-bias voltage is modulated by the applied EAE is mediated by the orientation and magnitude of the applied magnetic field. The EAE induced DC self-bias modulations exhibit non-linear behaviour in response to a superimposed MAE, such that the resulting DC self-bias

* Author to whom any correspondence should be addressed.

differs from an additive combination of the two effects alone Simultaneous application of the electrical and MAEs offers the possibility of further decoupling ion and electron dynamics in RF plasma sources, and represents an improvement over each approach in isolation.

Keywords: low temperature plasmas, magnetic asymmetry effect, tailored voltage waveforms, hollow cathode

1. Introduction

Control of charged particle dynamics in hollow cathode (HC) enhanced capacitively coupled plasma (CCP) sources are an area of growing interest [1–5]. The enhanced ionisation efficiency and high plasma densities ($\geqslant 1 \times 10^{18}$ m^{-3}) afforded by HC sources makes them a desirable geometry for applications ranging from plasma assisted surface modification [6–8], to low-power sources for spacecraft propulsion [9–12]. In HC enhanced CCP sources, the charged particle dynamics are primarily mediated through their interaction with potential of the sheath and that produced via surface biasing, where the former case is of particular significance for electrons [13–15] and the latter more significant for ions [16–18]. The DC surface biases are of particular importance in HC discharges as they mediate not only the ion flux incident upon electrode surfaces, but also the energy distribution of secondary electrons accelerated back into the plasma, which drive a significant proportion of the total ionisation rate [19–21].

For a reactor of equal electrode areas, any variations in the electron or ion flux incident up-on the powered electrode necessitates an equal and opposite variation incident upon the grounded electrode to maintain charge conversation [22]. In practice this results in the formation of a DC self-bias on the powered electrode to mediate the positive and negative particle fluxes [23, 24]. The value of this DC self-bias is typically mediated by the relative size of the current collecting areas of the powered and grounded electrodes [5, 25, 26] and, to a lesser extent, differences be-tween the electrode materials, their thermionic emission, and secondary electron emission coefficients [27–29]. The operation of plasma sources that are physically symmetric is typically confined to specifically designed, research-focused setups such as that described in [30]. As distinct from this, technological reactors are almost always physically asymmetric due to the presence of an electrically grounded vacuum chamber than surrounds the plasma source.

Control of the DC self-bias voltage is of particular interest as it enables modification of the ion flux and energy distribution incident upon plasma facing material surfaces [31–33]. Direct control of the DC self-bias voltage has historically been achieved through either applying a DC voltage to one of the electrodes [6, 34, 35], or by employing multi-harmonic tailored voltage waveforms to induce an electrical asymmetry effect (EAE) [36–40]. By adjusting the relative phase and amplitude of individual frequency components that comprise the waveform, it is possible to control the DC self-bias through a modulation of the sheath dynamics and spatio-temporal ionisation mechanisms [41–43]. Recently, indirect control of the DC self-bias voltage has also been achieved through the application of static magnetic fields to induce charged particle flux asymmetries through the magnetic asymmetry effect (MAE) [44–46]. The MAE employs spatially inhomogeneous magnetic confinement of the charged species adjacent to one or more electrode surfaces. Magnetised species experience a significant reduction to their cross-field transport, while parallel transport is largely unaffected, enabling directional and spatial control over the phase-averaged electron and ion fluxes incident upon the powered and grounded electrodes. Magnetic geometries which result in asymmetric phase-averaged charge collection at the powered and grounded electrodes therefore enforce a variation in the DC self-bias voltage to maintain quasineutrality in the bulk [47, 48]. In summary, the EAE and MAE both achieve control over the DC self-bias voltage through enforcing a separation in the phase-averaged electron and ion dynamics, and more generally through enforcing a mass differentiated response to applied electromagnetic fields. The EAE facilitates separate control of the ion and electron dynamics via a mass-selective response to the high frequency voltage harmonics [14, 22, 49]. In contrast, the MAE facilitates discrete control over ion and electron dynamics via a mass-selective magnetisation of the electrons within a given source dimension [44–46, 48]. However, relatively little is understood regarding the combined effect of EAE and MAE, which could be of significant interest for applications where enhance control capability is required.

In this work we use 2D fluid-kinetic simulations to demonstrate the combined application of the EAE and MAE in a CCP source [21, 32, 42, 50–56] and assess their impact upon the charged-particle dynamics. Descriptions of the numerical model, magnetic topologies, and tailored voltage waveforms employed, are provided in sections 2, 2.1 and 2.2, respectively. Unmagnetised operation of the hollow cathode source is presented in section 3.1. Characterisation of the MAE for a single 13.56 MHz frequency discharge in argon is presented in section 3.2. The mechanisms underlying this control are discussed with respect to the spatially resolved secondary electron confinement in section 3.3. Simultaneous application of the MAE and EAE is presented in sections 4 and 4.1, demonstrating an interaction between the MAE and EAE via the sheath and ionisation dynamics.

2. Methodology and simulation methods

The simulated hollow cathode source, presented in figure 1, employs an annular copper powered electrode surrounding

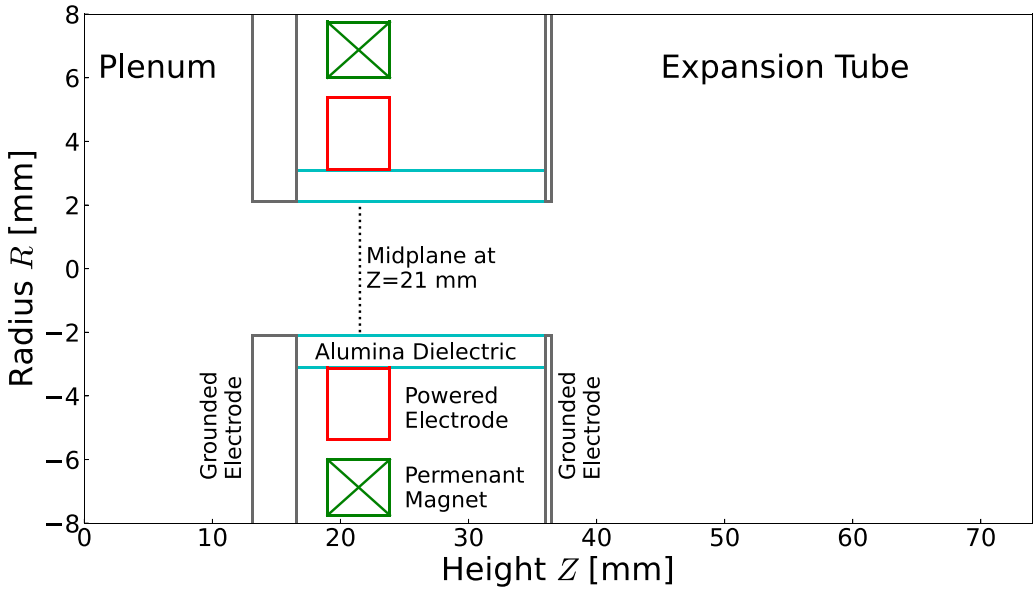

Figure 1. Illustration of the simulation domain used in this study. The domain is radially symmetric around $R = 0.0$ mm. Gas is introduced into the plenum and extracted at the end of the 40 mm expansion tube. An RF voltage is applied to the electrodes, denoted in red, power is coupled to the plasma through an alumina tube, denoted in blue. An annular permanent magnet is included co-axial with the powered electrode, denoted in green, and magnetic field vectors are shown in white. Dashed line at $Z = 21$ mm indicates the axial midpoint of powered electrode and permanent magnet.

an $R = 4.2$ mm inner-diameter alumina tube through which 100 sccm of argon gas is supplied [50, 52, 56]. During steady-state operation an axial pressure gradient forms between the upstream plenum at 200 Pa (1.5 Torr) and downstream expansion region at 113 Pa (0.85 Torr) as described in detail in previous work [21].

Two-dimensional, fluid-kinetic simulations were undertaken using the Hybrid Plasma Equipment Model (HPEM) [57]. A full description of the mesh and numerical methods applied can be found in [21, 32, 42], a brief summary is provided here. Within the model, bulk neutral, excited, and ionised species densities, fluxes and temperatures were obtained from solutions to mass, momentum, and energy conservation equations. Secondary electrons were treated by employing a Monte-Carlo kinetic model. Bulk electron flux was obtained from a Scharfetter–Gummel drift-diffusion model [58]. Bulk electron energy distributions were assumed to be Maxwellian and obtained via a two-term approximation of the Boltzmann equation. Mass and momentum were conserved at all plasma-facing material surfaces, but were not necessarily conserved across the inlet and outlet material boundaries to allow for gas flow. The energy continuity equation was bounded by a fixed outer boundary temperature of 325 K. Surface and volume charge densities were obtained via a semi-implicit solution to Poisson's equation, see [57], solved simultaneously with the continuity equations. The Poisson solution was bounded at the powered electrode by the time dependant RF voltage, $\phi_{\mathrm{RF}}(t) = \phi_0 \sin(\nu_{rf} t)$ for single frequency operation, or by equation (1) in multi-harmonic tailored waveform operation. Grounded electrodes and the outer boundary of the mesh were bounded as $\phi(t) = 0$ V.

The simulation mesh consisted of a rectilinear grid of 64×152 ($R \times Z$) cells in a cylindrically symmetric geometry, corresponding to a radial resolution of 0.125 mm per cell and an axial resolution of 0.5 mm per cell. An annular permanent magnet was included within the simulation domain, co-axial to the powered electrode ($Z = 21$ mm, $R = 6$ mm). The dashed line at $Z = 21$ mm in figure 1 indicates the axial midpoint of the co-axial powered electrode and permanent magnet. The hollow cathode source geometry was chosen due to its intrinsic physical asymmetry, as opposed to any externally applied electromagnetic asymmetry, where the grounded electrode area in contact with the plasma exceeds that of the powered electrode area. This physical asymmetry enforces the formation of a significant DC self-bias voltage on the alumina wall adjacent to the powered electrode, which forms to maintain current continuity through the source [23, 26]. Argon ions, accelerated through the DC self-bias enhanced sheath potential, undergo charge-exchange collisions with axially passing neutrals resulting in significant neutral gas heating within the powered electrode sheath [21, 52, 59, 60].

The argon plasma reaction mechanism considers Ar, Ar(4 s), Ar(4p), Ar(4d), Ar_2^*, Ar^+, Ar_2^+ and e^-, where the reaction mechanism is as described in [61]. The energy distribution functions for all gas-phase heavy-particle species were assumed to be Maxwellian, and were obtained from a two-term approximation of the Boltzmann equation. Gas-phase electron-neutral and electron-ion collisions include elastic, excitation and ionisation reactions [61]. Cascade processes, multi-step ionisation and heavy particle mixing between excited species are also included, the interaction cross-sections for which are obtained from [62–66]. Ion-neutral charge

exchange collisions are employed with a rate coefficient of 5.66×10^{-10} cm^{-3} s^{-1} $(T_g/300)^{0.5}$ where T_g is the neutral-gas temperature [67]. The sheath extension was calculated as in [42], where the radial sheath edge S_R is determined as the radius R that satisfies the Brinkmann criterion [68].

Ion induced secondary electrons were considered within the model. The secondary electron yield employed an energy independent model, with a secondary electron emission coefficient of 0.2 for alumina surfaces and 0.1 for metal surfaces. Secondary electron macroparticles were 'launched' from material surfaces with an initial energy of 3 eV and subsequently tracked in a similar fashion to a PIC model, accelerated by interpolated local electromagnetic fields. Secondary electrons employ the same reaction mechanism as the bulk electron population, and macroparticles that fell below 2 eV were returned to the bulk electron population. Electron induced secondary electron emission was not included within the model.

Electron cross-field transport was computed employing a thermal drift diffusion approximation, accounting for the Hall parameter limit perpendicular to the magnetic field [46]. This drift-diffusion approximation is then accounted for as a modification of the Scharfetter–Gummel flux in each cell. Due to the hollow cathode geometry, both magnetic topologies are predominately aligned parallel or anti-parallel to the alumina walls throughout the source region, see figure 1. The $v \times \mathbf{B}$ contribution to cross-field transport is therefore negligible due to the particular geometry of the source and topologies of the magnetic fields employed in this work. As such $\nabla \times \mathbf{B} \approx 0$ within the sheath and bulk regions, and therefore the $v \times \mathbf{B}$ contribution to cross-field transport is negligible.

2.1. Multi-frequency tailored voltage waveforms

The 'peak'-type tailored voltage waveforms investigated in this work are constructed employing a 13.56 MHz fundamental waveform and four additional harmonics with varying phase offsets employing equation (1):

$$\phi_{\mathrm{RF}}(t) = \sum_{k=0}^{n} \left(\frac{\phi_0}{n}\right) \sin\left(k\omega_0 t + \theta_k\right). \tag{1}$$

Here, $\phi_{\mathrm{RF}}(t)$ is the combined voltage waveform, ϕ_0 is its maximum amplitude, $\omega_0 = 2\pi\nu_0$ is the fundamental angular frequency, θ_k is the phase offset of harmonic k and n is the total number of applied harmonics. The shape and symmetry of the resulting waveform can be altered through varying the phase-offset between individual harmonics. However, due the intractable growth in the parameter space with increasing harmonic number, the same global phase offset θ is applied to each harmonic component, i.e. $\theta_k = \theta \; \forall \; k$. Examples of 'peak' and 'valley' voltage waveforms generated from equation (1) are presented in figure 2, where the peak and valley waveforms employ phase offsets of $\theta = \frac{\pi}{2}$ and $\theta = \frac{3\pi}{2}$, respectively.

Due to the phase-offset between successive harmonics, constructive interference leads to the formation of two large changes in voltage within each waveform. Notably, while the phase-averaged voltage remains zero for both waveforms, see figure 2, the positive and negative amplitudes vary such that $\phi_{\mathrm{RF}}^{+} \neq \phi_{\mathrm{RF}}^{-}$. This amplitude inequality, coupled with a non-instantaneous plasma response to the applied voltage, leads to the formation of an EAE, imparting a time-averaged DC bias voltage at the powered electrode. The 'magnitude' of the EAE produced via the application of an arbitrary tailored voltage waveform can be described through the symmetry parameter ϵ_s, which is determined via equation (2) following [36]:

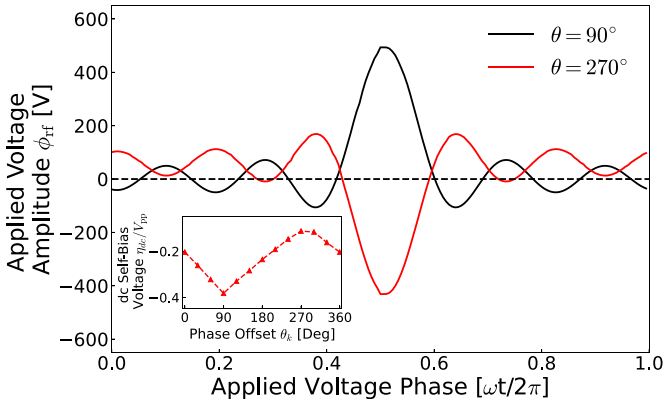

Figure 2. Examples of a two 'peak'-type tailored voltage waveforms employing phase offsets of $\theta = \frac{\pi}{2}$ and $\theta = \frac{3\pi}{2}$, respectively. Inlay: DC self-bias voltage modulation $\eta_{\mathrm{dc}}/V_{\mathrm{pp}}$ with respect to phase offset between $0° \leqslant \theta \leqslant 360°$ in a 600 V_{pp}, 13.56 MHz single frequency unmagnetised discharge.

$$\epsilon_s = \frac{\hat{n}_{Sp}}{\hat{n}_{Sg}} \left(\frac{Q_{Sg}}{Q_{Sp}}\right)^2 \left(\frac{A_p}{A_g}\right)^2 \frac{I_{Sg}}{I_{Sp}} \approx \left|\frac{\phi_{Sg}}{\phi_{Sp}}\right| \tag{2}$$

where, $\hat{n}_{Sp}$, $\hat{n}_{Sg}$ are the sheath averaged ion densities, Q_{Sg}, Q_{Sp} are the maximum electrode surface charges, A_p, A_g are the electrode surface areas, ϕ_{Sg}, ϕ_{Sp} are the maximum voltage drops across each respective sheath, where subscripts p and g denote the powered and grounded electrodes, respectively. The parameters I_{Sp} and I_{Sg} are represent the sheath integrals, defined as:

$$I_{Sx} = 2\int_0^1 \frac{n_i(x)}{\hat{n}_{Sx}} \xi \, \mathrm{d}\xi \qquad \text{where} \qquad \xi = \frac{x}{S_x} \tag{3}$$

where S_x is the maximum sheath extension. The DC self-bias voltage η_{dc} resulting from an EAE of magnitude ϵ_s, can be readily calculated through an application of Kirchhoff's law [69]. The result for the typical case where the change in voltage across the plasma bulk is very small is shown in equation (4)

$$\eta_{\mathrm{dc}} = -\frac{\phi_{\mathrm{RF}}^{+} + \epsilon_s \phi_{\mathrm{RF}}^{-}}{1 + \epsilon_s} \tag{4}$$

where, ϕ_{RF}^{+} and ϕ_{RF}^{-} are the maximum and minimum amplitudes of the applied voltage waveform respectively. Consistent with the typical design of technological plasma reactors, the surface area of grounded electrode in the geometry used here is larger than that of the powered electrode, which results in a negative DC self-bias voltage at the powered electrode.

It is important to state that equations (2) and (4), are only strictly valid for uniform sheaths adjacent to conducting surfaces, i.e. where the macroscopic plasma properties are uniform across metal electrode surfaces. In cases where plasma properties vary across one or more of the electrode surfaces, the local value of the DC self-bias may vary from the 'global' averaged value predicted by these equations due to surface charging. For the hollow cathode geometry employed in this work, the alumina dielectric layer covering the powered electrode prevents a DC current flow back to the power source. As a result, a net negative surface charge is maintained on the alumina surface, and the associated surface potential functions identically to a DC self bias [70]. The value of the surface charge is computed via the solution of Poisson's equation. Therefore, where referring to η_{dc} or the DC self-bias in this work, it is the DC potential associated with the alumina surface charge that is being referenced.

2.2. Magnetic asymmetry effect

The MAE facilitates the control of charged species dynamics via restricting or enhancing the charged particle flux to surfaces within a source or reactor [47, 71]. There are two general approaches to applying an MAE, (1) a homogeneous magnetisation of lighter particles (typically electrons) throughout a geometrically asymmetric source, i.e. where magnetic field lines are parallel to one charge collecting surface and perpendicular to the opposing charge collecting surface. This enforces a DC self-bias in proportion to the cross-field transport inhibition at the perpendicular charge collecting surface, facilitating a separation of the electron and ion dynamics. Or (2) a spatially varying magnetisation of one or more species adjacent to a single electrode, altering the charge balance to the surface. In practice the MAE is typically achieved with the former approach, via the inclusion of a static magnetic field adjacent to the powered electrode, while the species adjacent to the grounded electrode are left unmagnetised. For each approach, the topology and orientation of the field relative to the charge collecting surfaces also alters the effect. Fields normal to the charge collecting surface enforce an enhanced charge flux, while fields parallel inhibit the charge flux to the surface. A common arrangement employs a magnetron like geometry, with two co-axial magnetic rings or coils positioned behind a planar powered electrode. This results in localised electron confinement parallel to the electrode surface between the magnetic rings, and an enhancement of the plasma density adjacent to the powered electrode. In the absence of any other effect, simply altering the plasma density adjacent to one charge collecting surface while maintaining the plasma density adjacent to another, will introduce a DC bias into the system to maintain charged flux continuity [72].

This relatively simple picture does not, however, capture two key elements (1) that the magnetic topology adjacent to a planar magnetron is highly non-uniform, and hence the macroscopic plasma properties (such as those in equation (2)) will not be spatially uniform across the electrode surface. (2) The spatio-temporal sheath dynamics, which may not be uniform in time such as via the application of multi-harmonic voltage waveforms. With reference to point 1: for the geometry employed in this work the magnetic field is predominately parallel (or anti-parallel) to the alumina walls in-front of the powered electrode, see figures 3(a) and (b). This is strictly true for the converging case, in which the field is Z-aligned and parallel to the alumina walls for the entire powered electrode height. The diverging case exhibits a parallel alignment ($-Z$) downstream of $Z = 21$ mm and an anti-parallel ($+Z$) alignment upstream of $Z = 21$ mm with a null on-axis at $Z = 21$ mm. Whether the field is parallel or anti-parallel does not affect the uniformity of the sheath, rather if the field is parallel or perpendicular. With the exclusion of the narrow null region in the diverging case, the powered electrode sheath can be treated as approximately uniform across the majority alumina surface with respect to the magnetic field orientation.

With respect to point 2, which forms the focus of this work, during an RF cycle the sheath adjacent to electrode surfaces oscillates in phase with the applied voltage. The oscillation of the sheath is driven primarily by the repulsion of electrons from the surface as a negative potential is applied. During the positive part of the phase cycle, the sheath collapses and electrons are drawn out of the plasma bulk. The opposite happens at the grounded electrode to maintain charge continuity. For the sheath to move in sync with the applied voltage waveform, it therefore requires that the electrons adjacent to the electrode surfaces posses a significant degree of mobility. If the electron mobility perpendicular to an electrode surface is inhibited, for example by the application of an external parallel aligned magnetic field, the electrons response to the applied electrode voltage will be altered. In effect, the 'inertia' of the sheath can be altered through controlling the degree to which electron are free to move perpendicular to the sheath. Of specific relevance to this work, Trieschmann *et al* [71], studied the application of a dual frequency driving voltage on a magnetised parallel plate discharge employing a 1D PIC model, and found the magnetised sheath dynamics to play a critical role in the resulting ion energy distribution.

As noted, many existing MAE studies have focused on geometries similar to magnetrons, employing a magnetic field normal to the powered electrode in a parallel plate RF-CCP discharge [44, 45, 47, 48, 71, 72]. Such discharges are of significant interest to the sputtering community, but are topologically limited as all magnetic field lines terminate into the powered electrode surface. The hollow cathode geometry employed here enables axially-aligned magnetisation parallel to electrode surface inhibiting radial the electron flux towards the powered electrode. The magnetic topologies employed in this work are presented in figures 3(a) and (b); the magnetic field strength on-axis ($R = 0.0$ mm) for both topologies is shown in panel (c).

Two static magnetic topologies are studied in this work. The magnetic topology in figure 3(a) is achieved via the inclusion of a co-axial permanent magnet around the powered electrode, where the dipole is aligned axially as denoted by the red

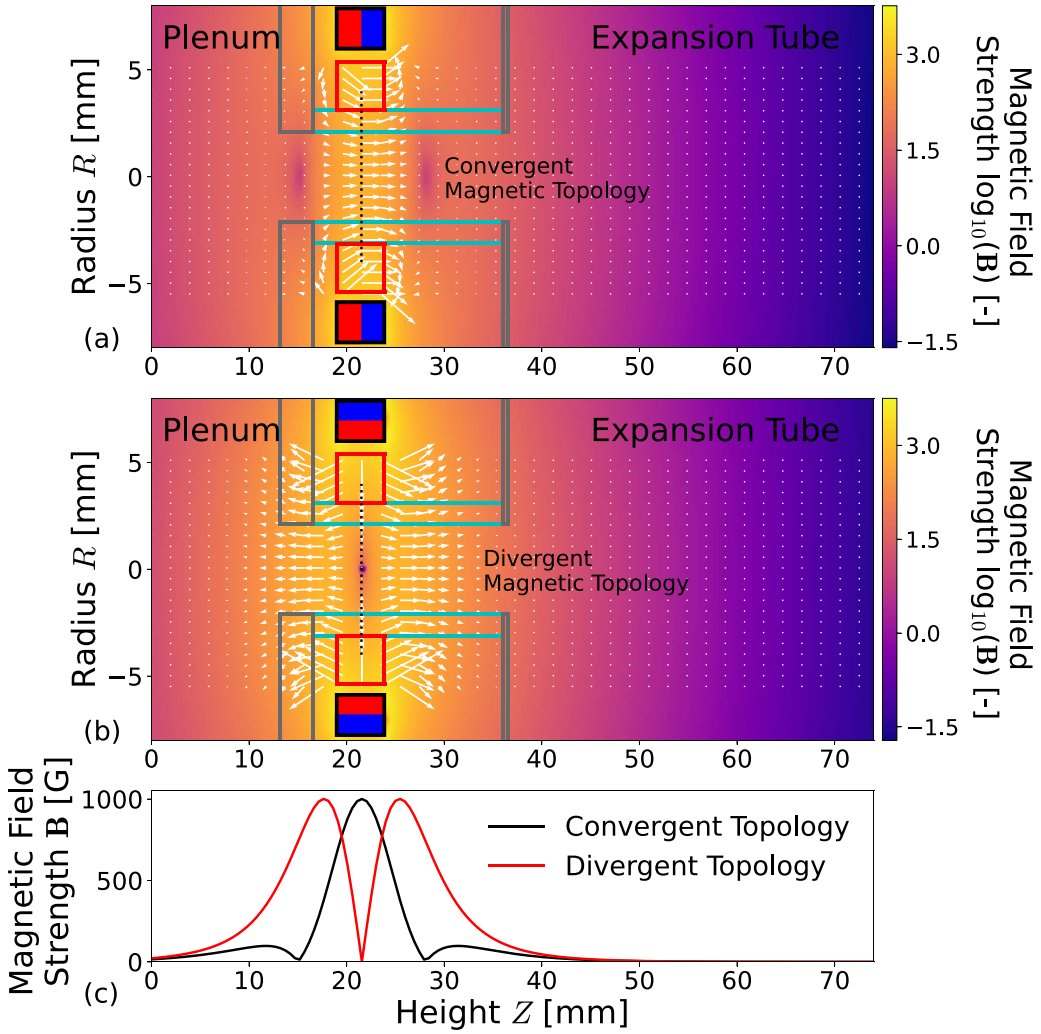

Figure 3. Illustration of the simulation domain (not to scale) showing the axially-aligned (a) convergent and (b) divergent magnetic topologies for a maximum on-axis magnetic field strength of 1000 G, panel (c) shows the magnetic field strength on-axis ($R = 0.0$ mm) for both topologies. The permanent magnet orientation is illustrated as the solid red and blue sections, denoting the north and south magnetic poles, respectively. Both magnetic topologies are both radially symmetric around $R = 0.0$ mm. The dashed line indicates the centre of the powered electrode at $Z = 21$ mm, for clarity.

(north) and blue (south) poles. This dipole orientation creates a $+Z$ orientated field across the diameter of the hollow cathode source tube, with maxima at the alumina surface adjacent to the powered electrode ($Z = 21$ mm). This henceforth denoted 'convergent' topology maximises the magnetic field adjacent to the powered electrode at $Z = 21$ mm, see black profile in figure 3(c), but not adjacent to the grounded collecting areas. The magnetic topology in figure 3(b) is achieved by rotating the permanent magnetic dipole by 90°, such that the north face of the magnet is facing radially inwards towards the plasma channel. This dipole orientation creates a divergent $\pm Z$ orientated field across the diameter of the source tube, with an on-axis minima in field strength at $Z = 21$ mm, see red profile in figure 3(c). Note that the field magnitude increases rapidly both upstream and downstream from this on-axis minima, with the field being aligned in the $+Z$ direction downstream and in the $-Z$ direction upstream. This henceforth denoted 'divergent' topology enforces a region of free-streaming electrons in the powered electrode sheath and the adjacent plasma bulk, but magnetises the electrons immediately up and downstream of the powered electrode. The effects of these topologies on the DC self-bias voltage and radial charged fluxes for a single 13.56 MHz discharge are presented in section 3.2.

A species can be considered magnetised if its Larmor radius is smaller than the source geometry (Larmor radius $r_L < R_{\text{source}} = 2.1$ mm). For the conditions studied here the bulk electron temperature does not typically exceed 4 eV [21]. Therefore the bulk electron population can be considered magnetised for field strengths above 35 G, assuming a thermalised velocity distribution. Secondary electrons released following ion bombardment are accelerated to significantly higher energies through the sheath normal to the alumina surface, i.e. perpendicular to the magnetic field lines in both magnetic topologies. Prior studies have demonstrated mean ion and electron energies in the range 60–100 eV for the operating conditions shown here [32]. Secondary electrons can therefore only be considered magnetised for magnetic field strengths between 130–160 G, assuming their velocity perpendicular

to the magnetic field to scale as $v_\perp = \sqrt{2E_k/m_e}$, where m_e and E_k are the mass and kinetic energy of electron, respectively. Note that these values represent the minimum field for an electron to be magnetised on-axis. Off-axis electrons must satisfy that their Larmor radius be smaller than the radial distance to the closest wall and hence the minimum field requirement increases towards the walls. Due to their significantly higher mass, and high perpendicular velocity, argon ions are never magnetised at any radius for the magnetic field strengths studied in this work. Magnetised electrons exhibit enhanced parallel-field (Z-aligned) transport and inhibited cross-field (R-aligned) transport, facilitating spatial control of the magnetised electron dynamics as distinct from the unmagnetised ion dynamics.

3. Magnetic asymmetry effect in a hollow cathode geometry

3.1. Single-frequency discharge without external magnetic field

An unmagnetised control case was simulated to provide a point of comparison for the magnetised discharges that follow. The electron density n_e, bulk electron ionisation rate ι_α, electric field strength E_{tot}, secondary ionisation rate ι_γ, radial electron flux Γ_e, and RF power density P_{RF} are presented in figures 4(a)–(e), respectively for an unmagnetised 300 V (600 V_{pp}), 13.56 MHz discharge in 200 Pa (1.5 Torr) of argon. Results are presented for the phase of most negative applied voltage (i.e. maximum sheath extent). The vector arrows in (c) denote both the electric field orientation and magnitude.

The electron density in figure 4(a) reaches a maximum of 1.5×10^{18} m^{-3} slightly upstream of the powered electrode ($Z = 18$ mm), reducing to $\approx 1.3 \times 10^{17}$ m^{-3} by the exit aperture at $Z = 37$ mm. The radial extent of the plasma bulk is widest adjacent to the downstream side of the powered electrode, $Z = 24$ mm, where both the on-axis plasma density and neutral density are lowest. The neutral argon density across the diameter of the source adjacent to the powered electrode ($Z = 21$ mm) ranges from 4×10^{22} m^{-3} to 1×10^{22} m^{-3}. This corresponds to neutral gas temperatures of 950 K on-axis, reducing to 800 K adjacent to the alumina wall. The ion-neutral mean-free-paths within the source vary from 0.3 to 0.6 mm, hence ions may undergo several collisions across the 4.2 mm diameter tube. The majority of the neutral gas heating arises from from ion-neutral charge exchange collisions within the sheath region. Ion diffusion to the walls is significantly enhanced due to the presence of a high DC self-bias voltage -0.26 V_{pp} (-159 V), localised to the alumina surface adjacent to the powered electrode ($Z = 19-24$ mm) [21]. The DC self-bias voltage also repels cool bulk electrons, resulting in a wider sheath adjacent to the powered electrode.

The bulk ionisation rate in figure 4(b) exhibits three discrete topological structures. The upstream and downstream structures reach maxima of 8.0×10^{22} m^{-3} s^{-1} and 1.0×10^{23} m^{-3} s^{-1}, respectively. The bulk ionisation rate is maximised at 1.2×10^{23} m^{-3} s^{-1} on-axis adjacent to the powered electrode, in line with the peak electron density at $Z = 18$ mm. Bulk electrons at this location are primarily accelerated by the sheath edge electric field during sheath expansion and collapse. The average (bulk plus secondary) electron temperature is maximised within the sheath at 15.5 eV, due primarily to the large secondary electron population. The maximum electron temperature on-axis is 3.9 eV, co-located with the downstream peak in bulk ionisation rate. The electron temperature at the region of maximum electron density is slightly lower at 3.2 eV.

The electric field at the phase of maximum sheath extent (i.e. most negative applied voltage) is shown in figure 4(c). The skin depth is approximately 40 mm, exceeding the radius of the tube, however the electric field topology is dominated by the sheath localised fields due primarily to the significant negative dc self-bias. The maximum electric field strength is 3.7×10^5 Vm^{-1} in the powered electrode sheath, and 1.0×10^5 Vm^{-1} and 0.7×10^5 Vm^{-1} in the upstream and downstream grounded sheaths, respectively. Electron heating is predominately driven during phases of sheath expansion, as the driving voltage becomes more negative, and sheath collapse when the driving voltage is most positive. Radial motion of the sheaths adjacent to the powered and grounded electrodes results in the three localised regions of bulk ionisation adjacent to each electrode [21]. As the skin depth exceeds the radius of the tube, a small ($\approx 1 \times 10^4$ Vm^{-1}) axially-oriented electric field is present within the plasma bulk. This field drives a relatively small axially aligned oscillating electron flux, but is negligible compared to the sheath-field enforced electron fluxes.

Secondary electrons, released through ion bombardment of the alumina surface, are accelerated back towards the plasma bulk at high, non-thermal energies (typically $\approx 10-100$ eV), representing an efficient additional ionisation mechanism [20, 29]. The secondary ionisation rate, shown in figure 4(d), is maximised on-axis at 2.2×10^{24} m^{-3} s^{-1}, reducing to $\approx 5 \times 10^{24}$ m^{-3} s^{-1} at the phase-averaged sheath edge. Secondary electrons accelerated through the powered electrode sheath have a mean energy of $\approx$60 eV, dependant upon the RF phase at which they are released. Due to their high velocity, and hence low collision cross-section compared to bulk electrons, secondary electrons are able to cross the plasma bulk and reflect from the opposite sheath, resulting in the peak secondary ionisation rate on-axis. While the maximum secondary electron ionisation rate is an order of magnitude higher than the maximum bulk ionisation rate, it represents just over half of the total volume-integrated ionisation, accounting for the greater volume within which bulk ionisation occurs.

The radial electron flux at the phase of most negative applied voltage is presented in figure 4(e), where the maximum radial electron flux occurs between the location of peak plasma density and the phase-averaged sheath edge. Note that the radial electron flux at this phase is orientated away from the alumina surface. This is due to the sheaths having just expanded, repelling electrons from the wall, and also the emission of secondary electrons, released normal to the wall surface. The RF power density is shown in figure 4(d) for the same phase. RF power deposition is computed as the product of the charged particle current density (i.e. the product of charge

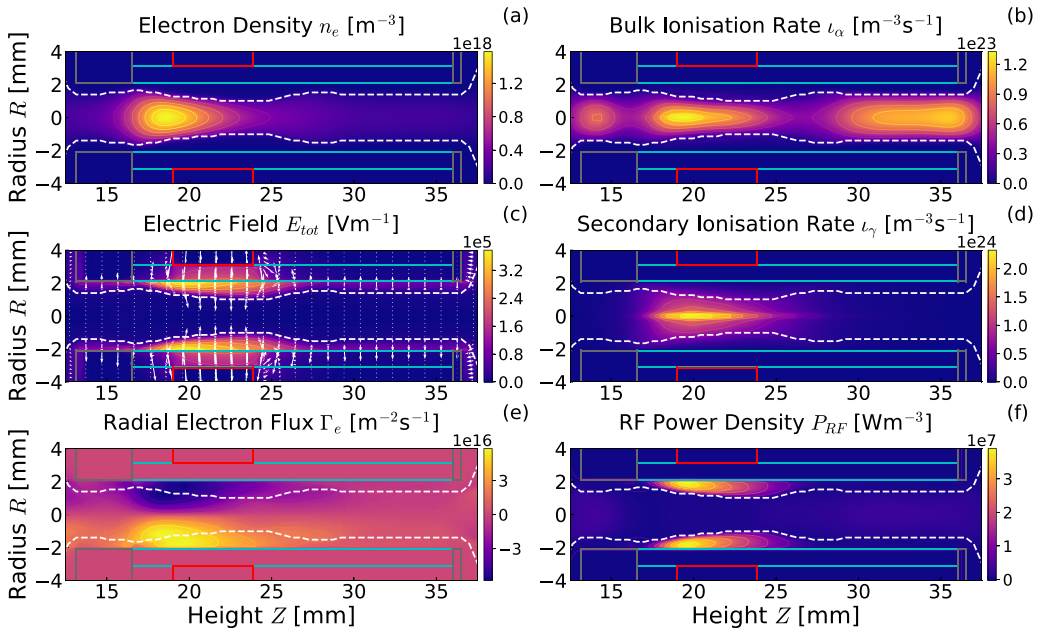

Figure 4. Spatial distribution of key macroscopic properties, including the (a) electron density, (b) bulk electron ionisation rate, (c) Electric field strength, (d) secondary electron ionisation rate, (e) radial electron flux, and (f) the RF power density, for an unmagnetised 300 V, 13.56 MHz discharge, plenum pressure: 200 Pa (1.5 Torr) of argon. Vector arrows in (c) denote electric field orientation and magnitude. The phase-averaged sheath extent is denoted by the white dashed lines for clarity.

and flux density) and the local electric field strength. Power is therefore maximised in the sheaths, reaching 38.6 Wcm^{-3} at adjacent to the alumina wall at the upstream edge of the powered electrode. This represents the maximum intersection between the regions of highest charged particle flux, see electron flux in figure 4(e), and electric field strength. The RF power deposition reduces downstream, to a maximum of 14.3 Wm^{-3} accompanied by a drop in electron density and flux, and a widening of the sheath and hence reduction in sheath electric field strength.

3.2. Magnetic control of the DC self-bias voltage

Prior to the application of tailored voltage waveforms, the MAE was first characterised for a 300 V, 13.56 MHz frequency reference case, with respect to varying magnetic field strength and topology. Here, and for the remainder of this work, the quoted magnetic field strengths represent the maximum on-axis ($R = 0$ mm) value, which are found at ($Z =$ 21 mm) for the convergent magnetic topology (figure 3(a)), and the ($Z = 23.5$ mm) for the divergent topology (figure 3(b)). Key macroscopic properties for the 1000 G convergent and divergent topology magnetised single frequency 13.56 MHz discharges are presented in figure 5(a)–(h). Aside from the externally applied magnetic field, the operating conditions are identical to the unmagnetised control case presented in figure 4, consisting of 300 V (600 V_{pp}), 13.56 MHz discharges in 200 Pa (1.5 Torr) of argon. Results are presented for the phase of most negative applied voltage (i.e. maximum sheath extent). The vector arrows in (c) and (d) denote both the electric field orientation and magnitude.

The application of an external magnetic field significantly alters the discharge topology. This is most apparent between the electron density distributions shown in figures 5(a) and (b) for the convergent and divergent magnetic topologies, respectively. The convergent magnetic topology enforces a wider and more axially homogeneous plasma bulk as compared to unmagnetised operation. The maximum on-axis plasma density is 1.6×10^{18} m^{-3} and the maximum on-axis electron temperature is 3.7 eV, both similar to the unmagnetised case. For an applied magnetic field of 1000 G, both the bulk and secondary electron populations are magnetised. The predominately Z-aligned convergent magnetic field does not inhibit axial electron transport within the source, however radial electron transport is inhibited. This restricts radial electron motion to within the sheaths (see figure 5(g)) where the radially-aligned sheath electric fields dominate the electron motion. As a result, secondary electrons released from the alumina wall are accelerated until they reach the sheath edge, where they are radially confined (see figure 5(c)), resulting in a radially narrow ring of enhanced secondary electron ionisation. This differs from the on-axis maximum secondary electron ionisation rate, typical of hollow cathode discharges, previously observed for unmagnetised operation in figure 4(d). Despite the variation in topology, the maximum secondary ionisation rate is not significantly altered, increasing by 10% over the unmagnetised case to 2.4×10^{24} m^{-3} s^{-1}. Note however, that while the volume specific secondary ionisation rate remains relatively constant, the total number of secondary ionisation events increases due to the larger ionisation volume, this is addressed in more detail in figure 7. The enhanced sheath-edge ionisation rate for the converging magnetic topology increases the plasma density adjacent to the sheath, reducing the maximum phase-averaged sheath width to 0.51 mm, and enhancing the maximum sheath electric field by 20% to 4.5×10^5 Vm^{-1}, shown in figure 5(e). Consequentially the electron

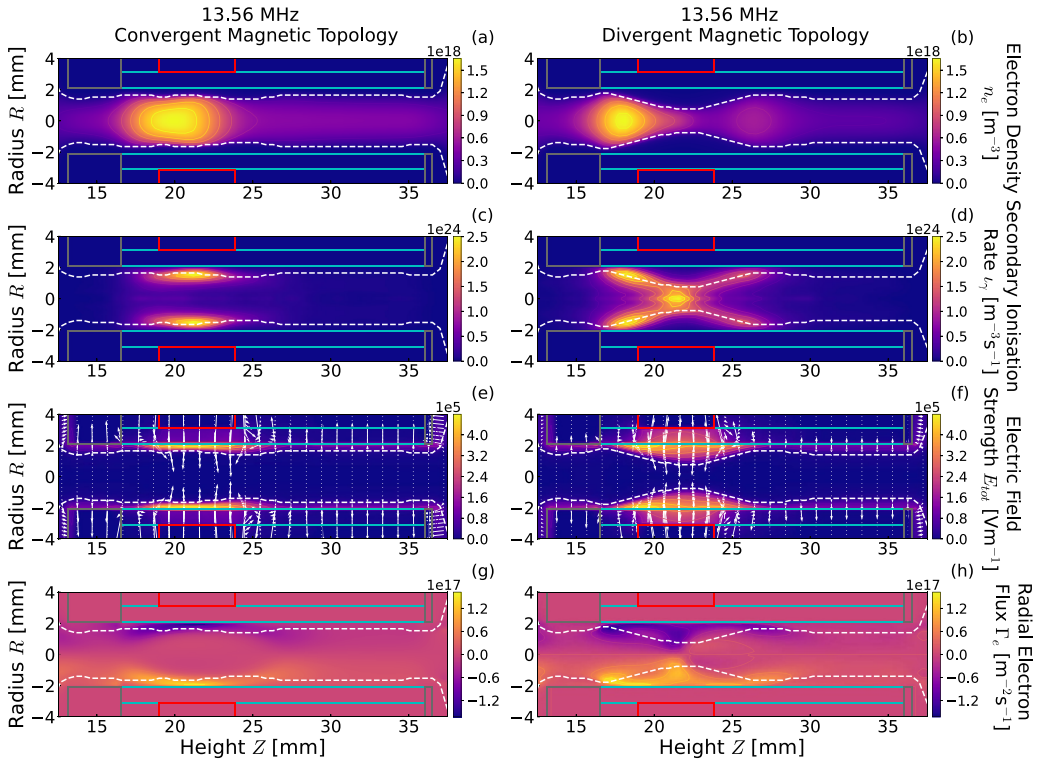

Figure 5. Magnetised single 13.56 MHz frequency discharges presenting the (a), (b) electron density, (c), (d) secondary ionisation rate (e), (f) electric field strength, and (g), (h) radial electron flux, for converging and diverging magnetic field topologies, respectively. Operating conditions: plenum pressure 200 pa (1.5 Torr) argon, 600 V_{pp} at 13.56 MHz, $B = 1000$ G employing convergent and divergent magnetic topologies. Vector arrows in (e), (f) denote electric field orientation and magnitude. The phase-averaged sheath extent is denoted by the white dashed lines for clarity.

and ion fluxes incident upon the alumina surface doubles relative to the unmagnetised case, from $\approx 5 \times 10^{22}$ m^{-3} s^{-1} to $\approx 1.2 \times 10^{22}$ m^{-3} s^{-1}. The ion and electron flux balance is discussed in more detail with respect to figure 6.

In contrast, the divergent magnetic topology enforces a 'pinching' of the plasma bulk along the mid-plane of the coaxial powered electrode and permanent magnet at $Z = 21$ mm, see figure 5(b). Here, the maximum on-axis electron density is reduced by 40% relative to the unmagnetised case, to 9.3×10^{11} m^{-3}, located slightly upstream of the powered electrode at $Z = 17$ mm. The downstream portion of the bulk exhibits a maximum electron density of 3.3×10^{11} m^{-3} at $Z = 27$ mm. This pinched topology arises due to the opposing dipoles of the ring magnet creating a magnetic null on-axis at $Z = 21$ mm, see figure 3(b). This null facilitates radial electron motion across the source at $Z = 21$ mm, but inhibits radial electron motion upstream or downstream of this plane. As a result, secondary electrons released at $Z = 21$ mm are capable of crossing the source tube exhibiting an on-axis maxima of 7.3×10^{23} m^{-3} s^{-1} in the secondary electron ionisation rate in figure 5(d). However, secondary electrons released upstream or downstream from this plane are radially confined to the sheath edge, as in the convergent magnetic case, and exhibit sheath edge localised maxima in the secondary electron ionisation rate and adjacent bulk electron density. As a consequence, the sheath exhibits an exaggerated curvature in proportion to the axially varying Z-aligned magnetic field strength, exhibiting a maximum phase-averaged sheath extension of 1.4 mm at $Z = 21$ mm and a minimum phase-averaged sheath extension of 0.2 mm at $Z = 17$ mm. The sheath electric field, see figure 5(f), correspondingly varies in inverse proportion to the sheath width, with a maximum sheath field of 3.1×10^5 Vm^{-1} upstream at $Z = 17$ mm reducing to a minimum of 2.4×10^5 Vm^{-1} at $Z = 21$ mm. Note, while the divergent magnetic topology facilitates increased radial electron transport out of the bulk through the $Z = 21$ mm plane, the reduced local electron density and sheath electric field results in a maximum radial electron flux of $\approx 5 \times 10^{22}$ m^{-3} s^{-1}, similar to the unmagnetised case.

The normalised DC self-bias voltage, η_{dc}/V_{pp}, computed from the RF phase-averaged surface charge at the alumina surface adjacent to the powered electrode ($R, Z = 2.1$ mm, 21 mm), is shown in figure 6(a). The radial electron Γ_e and argon ion Γ_{Ar^+} fluxes, integrated across the powered collecting surface, are shown in figure 6(b). The surface integrated powered to grounded electron and Ar^+ ratios, $\Delta\Gamma_e(\hat{R})$ and $\Delta\Gamma_{Ar^+}(\hat{R})$, respectively, are defined in equations (5) and (6), and are presented in figure 6(c). The dashed lines in figures 6(b) and (c) indicate the electron flux or electron flux ratio for unmagnetised operation, for ease of comparison.

The DC self-bias voltage in figure 6(a) exhibits an up-modulated response to the convergent magnetic topology and

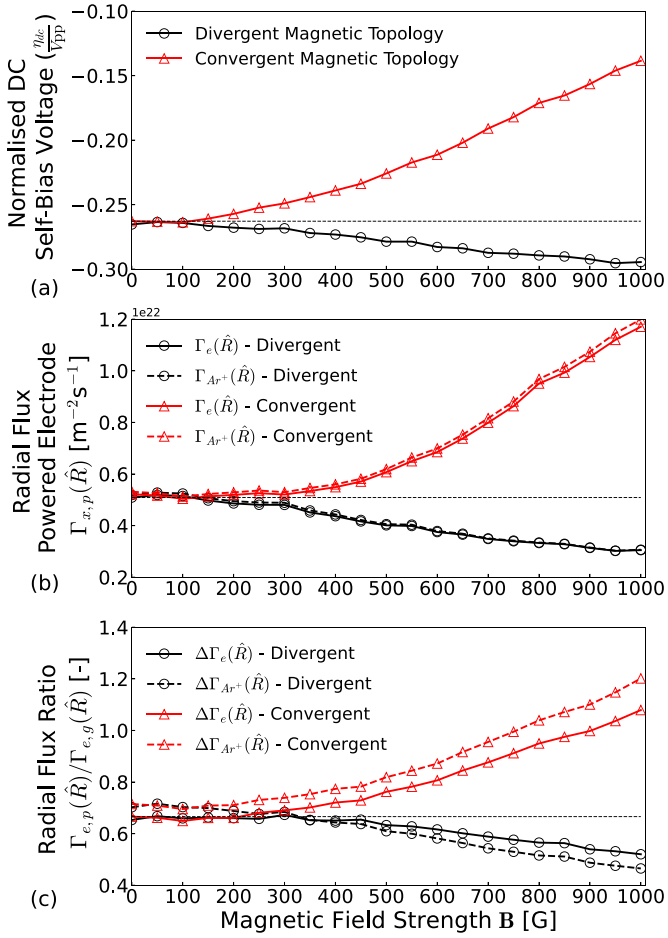

Figure 6. Normalised (a) DC self-bias voltage η_{dc}/V_{pp} calculated via the RF phase-averaged alumina surface charge, (b) the electron and ion fluxes incident on the alumina adjacent to the powered electrode, and (c) the surface integrated powered to grounded electron and Ar^+ radial flux ratios with respect to varying magnetic field strength and orientation. Dashed lines in (a) and (b) denote the conditions for an unmagnetised 600 V_{pp}, 13.56 MHz discharge for ease of comparison. Operating conditions: plenum pressure 200 pa (1.5 Torr) argon, 600 V_{pp} at 13.56 MHz, $0 \leqslant \mathbf{B} \leqslant 1000$ G employing convergent and divergent magnetic topologies.

a down-modulated response to the divergent magnetic topology. In both cases, no effects are observed for magnetic field strengths below ≈ 150 G, closely matching the minimum field required to magnetise secondary electrons, as discussed in section 2. The greatest degree of control is achieved for the converging case, exhibiting a $+0.13$ V_{pp} (78 V) variation in the DC self-bias, as compared to a -0.03 V_{pp} (18 V) variation for the divergent case. It should be noted that, as the pre-existing negative DC self-bias is already a large fraction ($\approx$53%) of the applied voltage amplitude, it will 'resist' further negative biasing of the alumina surface, partially accounting for the differing degrees of modulation. Least-squares fitting of the two DC self-bias trends with respect to increasing magnetic field (for magnetised cases between 150–1000 G) exhibits a best fit linear dependence on magnetic field ($\eta_{dc} \propto -2E^{-2}\,\mathbf{B}$, $R^2 = 0.97$) in the diverging case, and a quadratic best fit dependence on magnetic field ($\eta_{dc} \propto +6E^{-5}\,\mathbf{B}^2 + 2E^{-2}\,\mathbf{B}$, $R^2 = 0.99$), in the converging case, where **B** is in Gauss. The non-linearity in the converging topology indicates the presence of an additional intermediary feedback mechanism between the applied field and the DC self-bias, not present in the diverging topology.

The relative electron and ion flux incident on the walls is mediated by the magnetic field in two ways. Firstly, via a direct modification of the radial (magnetised) electron transport; enhancing electron transport parallel to the field and inhibiting transport perpendicular to the field, inhomogeneously altering the flux density incident on plasma facing surfaces depending upon their orientation to the applied field. Secondly, via a variation in the spatio-temporal sheath heating and/or additional $\mathbf{E} \times \mathbf{B}$ electron heating, such as the enhanced Hall current 'μ-mode' heating recently demonstrated by Eremin *et al* [73], leading to localised plasma density variations. Modification of the local electron and ion flux incident upon the powered, but not grounded, electrode via one or both of these mechanisms naturally alters the DC self-bias voltage.

The total electron and argon ion fluxes integrated across the powered charge collecting surface, i.e. the alumina surface between ($Z = 20$–25 mm), are shown in figure 6(b). The dashed line in figure 6(b) indicates the ion and electron flux for an unmagnetised case, for ease of comparison. Here, the electron and argon ion fluxes exhibit no significant change for either magnetic topology below $\approx$150 G. Above $\approx$150 G fluxes respond to the applied magnetic field, increasing by a factor of 2.5 by 1000 G in the convergent topology, and decreasing by a factor of 1.6 by 1000 G in the divergent topology. In both magnetic topologies the surface integrated electron and ion fluxes to the powered electrode remain closely coupled, with ion diffusion out of the plasma bulk being mediated by the change in DC self-bias. An increase in the electron flux incident upon the powered electrode in the convergent topology is perhaps unexpected, as the axial magnetic field inhibits radial transport at that location. However two effects counteract this, firstly and most importantly, the total power deposition increases from 2.2 W to 4.2 W resulting in a higher electron density and flux overall. This will be discussed in more detail with reference to figure 7. Secondly, the increasing electron flux to the powered electrode counteracts the existing physical asymmetry, which collects fewer electrons via a smaller powered electrode, resulting in the more positive DC self-bias voltage observed in figure 6(a). A more positive powered electrode surface results in lower energy electrons being able to cross the sheath, electrostatically enhancing the radial transport and counteracting the magnetic cross-field inhibition. Counter intuitively therefore, attempting to magnetically reduce the radial electron mobility in a hollow cathode geometry may instead result in an increased radial electron flux, due to an inhibition of the negative DC self-bias enforced by the physical asymmetry. Precisely how the electron radial transport is altered for a given source geometry and magnetic topology is therefore extremely important to determining the magnitude of the resulting MAE.

To quantify this behaviour further, it is worth examining the ratio of each species flux incident upon the powered and grounded charge collecting areas. Here a species flux ratio is defined as the total flux incident upon the powered collecting surface,

as shown in figure 6(b), divided by the total flux incident upon all of the grounded collecting surfaces ($Z = 14.5-20$ mm and $Z = 25-38$ mm). The electron and ion flux ratios are defined in equations (5) and (6)

$$\Delta\Gamma_e\left(\hat{R}\right) = \frac{\Gamma_{e,p}\left(\hat{R}\right)}{\Gamma_{e,g}\left(\hat{R}\right)}. \tag{5}$$

$$\Delta\Gamma_{\mathrm{Ar}^+}\left(\hat{R}\right) = \frac{\Gamma_{\mathrm{Ar}^+,p}\left(\hat{R}\right)}{\Gamma_{\mathrm{Ar}^+,g}\left(\hat{R}\right)}. \tag{6}$$

Here, $\Gamma_{e,x}(\hat{R})$ and $\Gamma_{\mathrm{Ar}^+,x}(\hat{R})$ are the phase-averaged radial electron and argon ion fluxes integrated across the 'x'th electrode surface area, where the powered and grounded electrodes are represented by 'p' and 'g', respectively. For $\Gamma_{e,x}(\hat{R})$ over unity, more electrons are incident on the powered electrode, for $\Gamma_{e,x}(\hat{R})$ under unity, more electrons are incident on the combined grounded electrode surfaces, a $\Gamma_{e,x}(\hat{R})$ of 1 indicates equal electron fluxes across both electrodes. Note that the ion-to-electron flux ratio incident on any single surface is always close to unity, as required for quasineutrality and as observed in figure 6(b). The electron flux ratio $\Delta\Gamma_e(\hat{R})$ and argon ion flux ratio $\Delta\Gamma_{\mathrm{Ar}^+}(\hat{R})$ are presented in figure 6(c) for both magnetic topologies in the range $0 \leqslant \mathbf{B} \leqslant 1000$ G.

Focusing first on the divergent magnetic topology, shown in black, the electron and argon ion flux ratios are again similar for field strengths below ≈150 G. Above this, both the electron and ion flux ratios decrease with increasing applied magnetic field strengths. A decrease in both ratios indicates a reduction in the total charged-particle flux incident upon the alumina adjacent to the powered electrode with increasing magnetic field strength. Notably, $\Delta\Gamma_e(\hat{R})$ decreases less rapidly with respect to magnetic field strength than $\Delta\Gamma_{\mathrm{Ar}^+}(\hat{R})$. This indicates that the electron flux incident upon the grounded collecting area is reducing less rapidly than the ion flux. The net effect is that the *relative* electron flux to the powered surface is increased, necessitating a more negative DC self-bias to maintain an equal ion flux, as observed in figures 3(a) and 6(a). The higher relative electron flux at the powered electrode arises due to reduced electron cross-field (radial) transport upstream and downstream of the powered electrode. Recall, the divergent magnetic topology minimises the magnetic field at the midpoint of the powered electrode, and maximises the magnetic field upstream and downstream of the powered electrode, see figure 3(c). These fields inhibit the radial diffusion of electrons not immediately adjacent to the powered electrode, leading to a lower radial electron flux at that location, and a relatively higher flux at the axial location of lower magnetic field strength.

Conversely, the convergent magnetic topology, shown in red, exhibits an increase in both the electron and argon ion flux ratios for increasing magnetic field strengths over 150 G. Unlike the diverging topology, the difference between the electron and ion flux ratios remains approximately the same with increasing magnetic field strength. Above ≈800 G, the trend in the convergent fluxes changes slope, growing at a reduced rate. This transition is also observed for the convergent trends in figures 6(a) and (b) and occurs as the powered-to-grounded flux ratios reach and exceed unity. At this point a larger total charged-particle flux is incident upon the smaller powered electrode area than the comparatively larger combined grounded electrode areas. This arises due to a confinement of the secondary electrons adjacent to the powered electrode, significantly increasing the local ionisation rate and plasma density.

3.3. Secondary electron dynamics and cross-field transport

Ionisation within the hollow cathode source predominately arises through direct secondary electron impact events. These kinetically treated secondary electrons are accelerated radially through the powered electrode sheath, following ion bombardment of the alumina surface, resulting in a significant ionisation rate on-axis, as shown previously in figure 4(d). Introducing an axially aligned external magnetic field, either in the converging or diverging configuration, will alter the secondary ionisation by spatially restricting the secondary electron mobility across the hollow cathode source.

To examine this, the radially resolved secondary ionisation rate ι_γ is presented in figures 7(a) and (b), for converging and diverging magnetic orientations respectively. Here the secondary electron ionisation rate adjacent to the powered electrode at $Z = 21$ mm is presented across the source channel between $R = -2.1$ mm to $R = 2.1$ mm, i.e. radially across the magnetic extrema in figure 3. These are presented for maximum on-axis magnetic field strengths between 0 and 1000 G in a 300 V, 13.56 MHz single frequency discharge as before. The radially integrated secondary electron ionisation rate $\Sigma\iota_\gamma$ is calculated as the total number of secondary ionisation events (i.e. the product of the secondary ionisation rate and cell volume) per time, integrated radially (between $R = -2.1$ mm to $R = +2.1$ mm) at the axial midpoint of the powered electrode ($Z = 21$ mm). Both $\Sigma\iota_\gamma$ and the total volume integrated RF power deposition P_{RF} are presented in figure 7(c). The phase-averaged sheath extent is denoted by the dashed lines in figure 7(a) and (b) for clarity.

The radially resolved secondary electron ionisation rate adjacent to the powered electrode at $Z = 21$ mm is presented in figure 7(a) for the convergent magnetic topology. The maximum secondary electron ionisation rate remains on-axis for magnetic field strengths below ≈150 G, consistent with the hollow cathode effect [5, 20]. For magnetic field strengths above this value, the secondary electron ionisation rate on-axis begins to reduce, while the secondary ionisation rate adjacent to the sheath edge increases, where the sheath edge is denoted by the white dashed lines. For magnetic field strengths in excess of 400 G, the majority of ionisations occur adjacent to the sheath edge at radii $R \geqslant 1$ mm. Note that the ionisation rates are presented with respect to volume and, due to the cylindrical geometry, the absolute ionisation rate is significantly higher at higher radii even if the peak volume specific rate is similar. This behaviour arises due to the magnetisation of the secondary electron population. Within the sheath, secondary electron dynamics are electrostatically dictated due to the

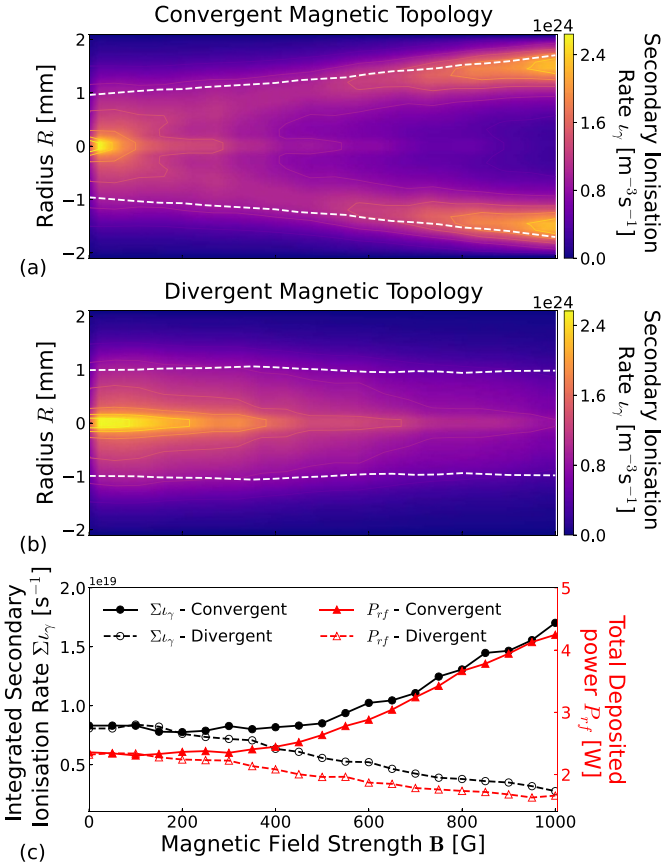

Figure 7. Radially resolved secondary electron ionisation rates ι_γ across the axial centre of the powered electrode at $Z = 21$ mm for (a) a convergent magnetic topology, and (b) a divergent magnetic topology, with respect to magnetic field strength. Subplots (a) and (b) share the same horizontal axis as subplot (c). Radially integrated (c) secondary electron ionisation rate $\Sigma\iota_\gamma$ along $Z = 21$ mm between $R = -2.1$ mm to $R = +2.1$ mm and total deposited RF power P_{RF}. The dashed lines in (a) and (b) denote the phase-averaged sheath extent. Operating conditions: plenum pressure 200 pa (1.5 Torr) argon, 600 V_{pp} at 13.56 MHz, $0 \leqslant \mathbf{B} \leqslant 1000$ G.

high radial electric field. Beyond the sheath, the radial electric field strength reduces and the secondary electron dynamics is instead dictated by the magnetic field. The majority of secondary electrons are confined to narrow regions of equi-magnetic-potential, within one or two Larmor radii of the sheath edge, leading to high collision and ionisation rates.

The radially integrated secondary ionisation rate $\Sigma\iota_\gamma$ across $Z = 21$ mm between, $R = -2.1$ mm to $R = 2.1$ mm, is shown in figure 7(c). Recall, this represents the total volume-integrated number of secondary ionisation events through the axial plane at $Z = 21$ mm. Focusing first on the convergent magnetic geometry, denoted in black; the radially integrated secondary ionisation rate increases with applied magnetic field strength varying by 51%, from $\Sigma\iota_\gamma = 8.32 \times 10^{18}$ s^{-1} to 1.70×10^{19} s^{-1}, over the range $0 \leqslant \mathbf{B} \leqslant 1000$ G. This enhanced sheath-edge localised ionisation increases the local plasma density, which reduces the phase-averaged sheath extent. The phase-averaged sheath extent reduces 65%, from 1.14 mm to 0.40 mm over the same magnetic range. This reduction enhances the electric field across the sheath, and increases the total RF power deposited into ions and secondary electrons by 45%, from 2.36 W to 4.25 W, as presented in figure 7(c). The reduced phase-averaged sheath extent also increases the capacitance of the powered electrode sheath, reducing the DC self-bias as observed previously in figure 6(a).

The combination of a reduced phase-averaged sheath extent, steeper sheath electric field gradient, and enhanced sheath edge localised ionisation due to secondary electron magnetisation significantly increases the plasma density and hence radial ion and electron fluxes incident on the alumina wall adjacent to the powered electrode. This feedback mechanism between the increased radial magnetic confinement and higher sheath localised secondary ionisation rate agrees with the previously observed enhanced electron to ion flux ratio to the powered electrode in figure 6(b). In summary, the converging magnetic topology negates the expected reduction in radial electron transport by enhancing the sheath edge ionisation and reducing the travel distance to the point of ionisation to the wall adjacent to the powered electrode.

Sheath localised ionisation is not observed for the diverging magnetic topology, see figure 7(b). Here the location of maximum secondary electron ionisation rate remains on-axis for all applied magnetic field strengths in the range $0 \leqslant \mathbf{B} \leqslant 1000$ G. This is expected as secondary electrons crossing the hollow cathode channel at $Z = 21$ mm pass through a magnetic null on-axis at $R = 0$ mm, and therefore experience little-to-no cross-field transport inhibition. Electrons travelling across the hollow cathode channel further upstream or downstream from the powered electrode will experience radial confinement and a reduction in radial transport, see figure 3(c). Magnetised electrons upstream or downstream of $Z = 21$ mm will either undergo a collision in the bulk, or drift towards $Z = 21$ mm where they may again travel radially. Therefore it is most probable that any electrons lost via radial transport out of the bulk will be lost adjacent to the powered electrode. Any increase in the electron flux adjacent to the powered electrode necessitates an increase in the positive ion flux to maintain quasineutrality and therefore enforces a more negative DC self-bias voltage, as observed previously in figure 6(a). Returning to figure 7(b), an approximately linear 66% reduction in the radially integrated secondary ionisation rate is observed, from $\Sigma\iota_\gamma = 8.07 \times 10^{18}$ s^{-1} to 2.76×10^{19} s^{-1}, with a corresponding 28% reduction in the deposited RF power shown in figure 7(c). These effects arise due to an increasing sheath width and reduced sheath electric field, the opposite to that observed in the converging magnetic topology. The reduced ionisation adjacent to the powered electrode again agrees with the reduced powered to grounded ion flux ratio trends observed previously in figure 6(b). In summary, the divergent magnetic topology acts to increase the probability that electrons are lost to the wall adjacent to the powered electrode through reducing the radial transport immediately upstream and downstream the powered electrode.

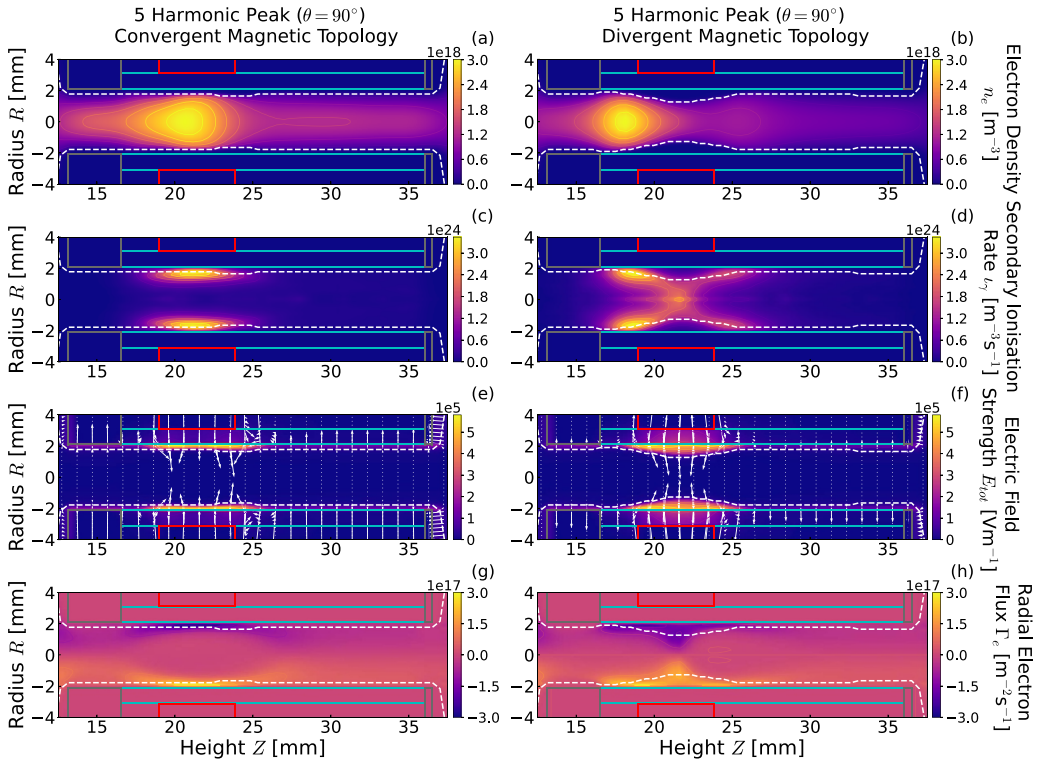

Figure 8. Magnetised 5 harmonic peak-type waveform powered discharges presenting the (a), (b) electron density, (c), (d) secondary ionisation rate (e), (f) electric field strength, and (g), (h) radial electron flux, for converging and diverging magnetic field topologies, respectively. Operating conditions: plenum pressure 200 pa (1.5 Torr) argon, 600 V_{pp}, $B = 1000$ G employing convergent and divergent magnetic topologies. Vector arrows in (e), (f) denote electric field orientation and magnitude. The phase-averaged sheath extent is denoted by the white dashed lines for clarity.

4. Simultaneous electrical asymmetry effect and magnetic asymmetry effect

The application of a 'peak'-type tailored voltage waveform enables a direct modification of the DC self-bias voltage η_{dc} via the EAE, specifically by varying the phase offset θ of the upper harmonics [74]. The effect of simultaneously applying an EAE and MAE will now be investigated, comparing to the behaviour exhibited by the MAE alone, presented previously. Key macroscopic properties for the 1000 G convergent and divergent topology magnetised single frequency 13.56 MHz discharges are presented in figures 8(a)–(h). Aside from the multi-harmonic driving voltage, operating conditions are identical to the magnetised single 13.56 MHz cases presented in figure 5, consisting of 300 V (600 V_{pp}) discharges in 200 Pa (1.5 Torr) of argon. The vector arrows in (c) and (d) denote both the electric field orientation and magnitude.

The electron density, secondary electron ionisation rates, and electric field distributions for the magnetised 5 harmonic peak-type discharges in figure 8 are topologically similar to those previously observed for the single 13.56 MHz driven discharges in figure 5. The convergent magnetic topology enforces a radially broad plasma bulk with a maximum electron density of 3.0×10^{18} m^{-3} on-axis at $Z = 21$ mm. The electron density reduces to 1.2×10^{18} m^{-3} downstream of the powered electrode, and extends beyond the exit aperture of the source at $Z = 37$ mm. Here, the divergent topology discharge exhibits a similar 'pinched' bulk electron density distribution, with a similar maximum density of 2.5×10^{18} m^{-3}, located on-axis at $Z = 17$ mm. This differs from magnetised single frequency operation, where the maximum electron density in the diverging case was significantly lower than the converging case. Both magnetic topologies exhibit similar distributions in the secondary electron ionisation rates as compared to the magnetised single-frequency discharges, with maximum sheath-adjacent secondary ionisation rates of 3.3×10^{24} m^{-3} s^{-1} and 1.8×10^{24} m^{-3} s^{-1} for the convergent and divergent topologies, respectively. The higher secondary electron ionisation rates and electron densities for the multi-harmonic driven discharges enforce narrower sheaths for both magnetic topologies, with a minimum This is most apparent in the divergent topology where the maximum phase averaged sheath extent between $Z = 18$ mm to $Z = 25$ mm is only 0.9 mm, as compared to 1.4 mm for the 13.56 MHz discharge. Consequentially the maximum sheath electric field varies less over the same axial range for the multi-harmonic discharges, as compared to the single-frequency discharges. The reduced variation in sheath extent and field, i.e. 'stiffer' sheaths, reduces the impact of multi-harmonic waveform tailoring, and hence will influence the discharge dynamics and degree of control afforded over the DC self-bias voltage.

The normalised DC self-bias voltage η_{dc}/V_{pp} at the alumina surface adjacent to the powered electrode ($R, Z = 2.1$ mm, 21 mm) is presented in figures 9(a) and (b), for discharges

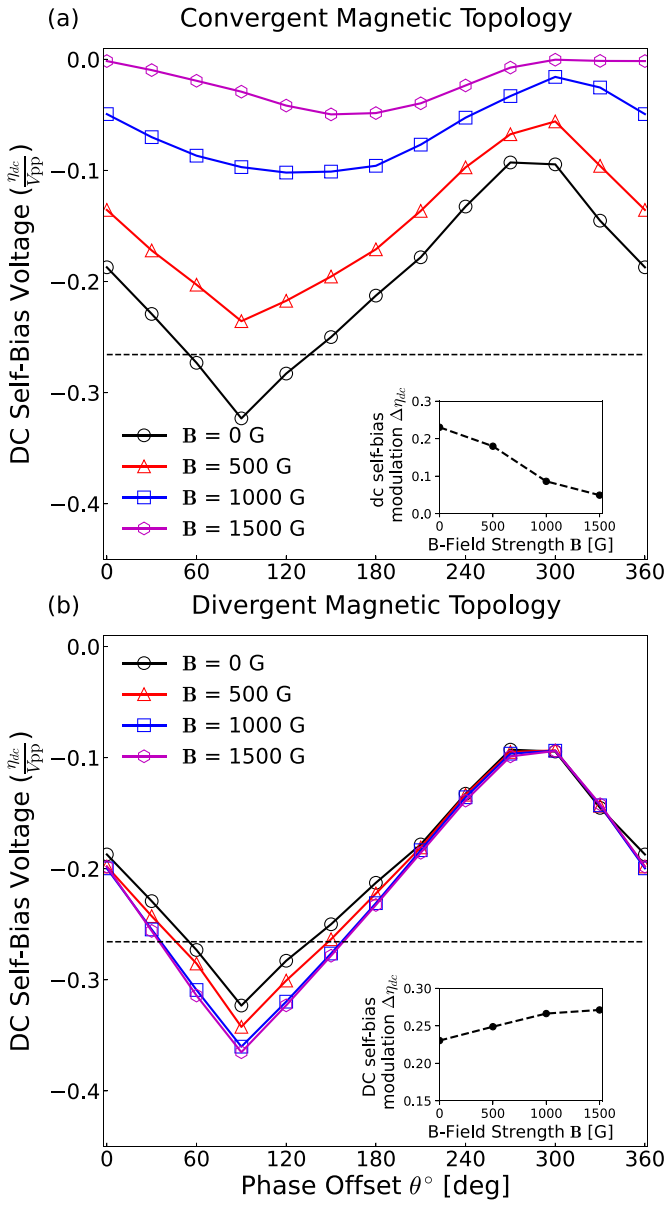

Figure 9. Normalised DC self-bias voltages η_{dc}/V_{pp}, calculated via the RF phase-averaged alumina surface charge, at the alumina surface adjacent to the powered electrode ($R,Z = 2.1$ mm, 21 mm) for four 600 V_{pp}, 5 harmonic peak-type waveform discharges, with phase offsets in the range $0^\circ \leqslant \theta \leqslant 360^\circ$, employing (a) convergent and (b) divergent magnetic topologies. Inlay: DC self-bias modulation $\Delta\eta_{dc}$, for each magnetic field strength. The DC self-bias voltage for an unmagnetised 600 V_{pp}, 13.56 MHz discharge is denoted by the dashed lines in (a) and (b), for clarity. Operating conditions: plenum pressure 200 pa (1.5 Torr) argon, 600 V_{pp}, magnetic field strengths between $0 \leqslant \mathbf{B} \leqslant 1000$ G.

employing 600 V_{pp}, 5 harmonic 'peak'-type voltage waveforms with phase offsets between $0^\circ \leqslant \theta \leqslant 360^\circ$ (see figure 2) and convergent and divergent magnetic topologies, respectively. The normalised DC self-bias voltage for an unmagnetised 600 V_{pp}, 13.56 MHz discharge is denoted by the dashed lines in (a) and (b) as a baseline for comparison. The DC self-bias voltage modulation $\Delta\eta_{dc}$ is presented in the inlay of (a) and (b), where $\Delta\eta_{dc}$ is computed as the difference between the maximum and minimum DC self-bias voltage over the full phase-offset scan.

The DC self-bias modulation for operation employing a 5 harmonic 'peak'-type waveform with phase offsets in the range $0^\circ \leqslant \theta \leqslant 360^\circ$ in an unmagnetised discharge is shown by the solid black lines in figures 9(a) and (b). Here the DC self-bias voltage is modulated by 23% (138 V), between -0.32 V_{pp} for $\theta = 90^\circ$ and -0.09 V_{pp} for $\theta = 270^\circ$. This modulation arises via a direct variation of the phase-resolved sheath dynamics, the related spatio-temporal ionisation dynamics and hence the electron and ion fluxes adjacent to and incident upon the powered and grounded electrodes, as has been discussed in detail in previous works [37, 38, 41, 74].

Of interest to this work is the extent to which the EAE induced dc self-bias modulation is affected by the MAE induced dc self-bias modulation when applied simultaneously. Operation in a convergent magnetic topology, figure 9(a), results in up-modulated DC self-bias voltages compared to the unmagnetised cases. The influence of the MAE on the EAE is most pronounced for phase offsets between $0^\circ \leqslant \theta \leqslant 180^\circ$, i.e. those that result in the most negative DC self-bias voltages. The phase offsets resulting in the most negative and positive DC self-bias voltages exhibit a shift from $\theta = 90^\circ$ and $\theta = 270^\circ$, respectively, for an unmagnetised discharge to $\theta = 150^\circ$ and $\theta = 300^\circ$, respectively for a 1500 G discharge. The most negative DC self-bias voltage is found to increase by $+0.28V_{pp}$ (168 V), from $-0.33V_{pp}$ to $-0.05V_{pp}$, more than double the $+0.13V_{pp}$ (78 V) increase observed for single frequency MAE operation under the same conditions in figure 6(a). This observation, alongside the shift in phase offsets resulting in the DC self-bias extrema in figure 6(a), indicates an interaction between the MAE and EAE beyond a simple linear addition of their respective DC self-bias modulations.

For the convergent magnetic topology, increasing the applied axial magnetic field results in a localised increase in the secondary ionisation rate adjacent to the sheath, and a subsequent reduction in the phase-averaged sheath extent—presented previously in figure 7. This inhibits the sheath mobility as the sheath edge is now more 'stiff' in response to an applied voltage. This in-turn interferes with the EAE's capability to modulate the sheath width, and hence the sheath capacitance, and ultimately reduces the EAE DC self-bias modulation from 23% (138 V) for an unmagnetised discharge to only 9% (54 V) for 1500 G on-axis convergent topology as shown in figure 9(a). Note also, that the DC self-bias is reduced to zero in the 1500 G convergent topology for phase offsets between $300^\circ \leqslant \theta \leqslant 360^\circ$, where the combined MAE and EAE effectively negate the existing HC physical asymmetry.

Operation in a divergent magnetic topology, presented in figure 9(b), results in significantly different behaviour to the convergent topology. Here, the EAE is largely unaffected by the applied magnetic field, exhibiting a slight reduction in the most negative DC self-bias between approximately $0^\circ \leqslant \theta \leqslant 180^\circ$, and almost no change to the EAE is observed for phase offsets between $210^\circ \leqslant \theta \leqslant 330^\circ$. No shifts in the phase offsets resulting in the extrema in DC self-bias voltage are observed, and the most negative DC self-bias voltage is down-modulated by only $-0.04V_{pp}$. This almost exactly

agrees with the $-0.03V_{pp}$ modulation achieved via single frequency MAE operation presented in figure 6(a), indicating no significant interaction between the EAE and MAE for the diverging magnetic topology. As noted previously with reference to figure 7(b), the MAE driven negative DC self-bias arises due to an increase in the probability that electrons are lost to the wall adjacent to the powered electrode, rather than immediately up and downstream of it. This will result in a widening of the sheath adjacent to the electrode, but will not significantly alter the sheath's capability to respond to the applied EAE, unlike the converging topology. As such, the combined EAE and divergent MAE exhibits both the most negative DC self-bias, and the largest DC self-bias modulation of $0.28V_{pp}$ (168 V) from $-0.09V_{pp}$ to $-0.37V_{pp}$ at 1500 G.

From figures 9(a) and (b) it is concluded that the MAE, introduced via an externally applied magnetic field, will interact non-linearly with a superimposed EAE. For the hollow cathode geometry studied here, maximising the magnetic field on-axis aligned with the powered electrode was found to strongly inhibit the control achieved by the EAE, while maximising the magnetic field on-axis away from the powered electrode slightly enhanced the control afforded by the EAE alone. It may be generalised that the interaction, if any, between the MAE and EAE is highly dependant upon the source geometry and applied magnetic topology.

4.1. Magnetised sheath and ionisation dynamics

The results previously shown in figures 9(a) and (b) suggest that the magnetic field strength and orientation significantly alter the control afforded by the EAE on the DC self-bias. This control has been attributed to the magnetisation and confinement of secondary electrons adjacent to the sheath edge, demonstrated by figures 7(a) and (b), which increases the plasma density adjacent to the sheath. To examine temporal variations in the plasma response leading to this effect, phase-resolved images of the bulk ionisation rate integrated through the source tube ($Z = 12 - 37$ mm), and the sheath dynamics adjacent to the powered electrode ($Z = 21$ mm) are presented in figure 10 for single frequency 13.56 MHz and multi-frequency 'peak'-type discharges. The phase-resolved ionisation structures for three single frequency 600 V_{pp}, 13.56 MHz discharges employing: no external magnetic field, a 1000 G convergent field, and a 1000 G divergent field are presented in figures 10(a), (c) and (e), respectively. The phase-resolved ionisation structures for three 600 V_{pp}, 5 harmonic 'peak'-type tailored voltage waveforms, described by equation (1) employing a phase offset of $\theta = \pi/2$, for the same magnetic topologies are presented in figures 10(b), (d) and (f). The $\theta = \pi/2$ 'peak' shaped waveform was chosen as it represents the most negative DC self-bias in both the converging and diverging magnetic topologies. The phase-resolved alumina surface potential adjacent to the powered electrode ($R, Z = 2.1$ mm, 21 mm) is presented for 13.56 MHz, and 'peak'-type operation in figures 10(g) and (h), respectively.

The unmagnetised single and multi-frequency cases in figures 10(a) and (b), exhibit periodic sheath collapse ionisation structures, denoted A_1, aligning with the most positive applied voltage, and a constant on-axis secondary ionisation structure, denoted C. Note that radial profiles are taken at the midplane of the powered electrode ($Z = 21$ mm), at the axial location of peak secondary electron ionisation, see figure 4(d), but slightly downstream of the region of peak bulk electron ionisation, see figure 4(b). The sheath collapse structures are radially extended as electrons move from the bulk and are lost at the radial walls during sheath collapse. The radial extension is more prominent for the peak waveform in due to higher radial electron flux necessitated during the shorter period of sheath collapse. The on-axis maximum in secondary electron ionisation is typical of hollow cathode operation where high energy secondary electrons undergo multiple reflections from the radial sheaths, as observed previously in figure 4(d). The sheath edge mirrors the waveform shape in both cases, exhibiting a sinusoidal variation over 0.78 mm for the 13.56 MHz waveform and a rapid variation over 0.52 mm for the peak-type waveform. Ionisation adjacent to, and within, the sheaths is two orders of magnitude lower than in the bulk due to the significantly reduced sheath averaged electron density. The sheath dynamics and ionisation structures exhibited by the unmagnetised cases are consistent with previous works in this source [21, 32, 74].

The application of a 1000 G on-axis convergent magnetic field significantly alters the sheath and ionisation dynamics, as presented in figures 10(c) and (d). Notably, the previously singular sheath collapse ionisation structures are radially elongated and break into multiple sub-structures, denoted A_1, A_2. This can be explained as the radially confined electrons not traveling the full distance between the bulk region about $R = 0$ mm and the radial wall during the relatively short period of sheath collapse. Therefore, the electrons lost during sheath collapse must originate only a few Larmor radii from the sheath edge. Ionisation due to secondary electrons is also shifted off-axis with a peak rate adjacent to the sheath edge, agreeing with the trends exhibited in figure 7(a). The enhanced sheath collapse and secondary electron sheath edge ionisation reduces the single frequency driven mean sheath extent by 0.35 mm, and the peak-type driven mean sheath extent by 0.33 mm. The enhanced sheath edge localised ionisation and narrower sheath extent result in a more rapidly collapsing sheath and an enhanced radial electron flux immediately adjacent to the wall, producing the off-axis sheath collapse ionisation structures at A_2. The surface potential of the radial alumina wall, shown in figures 10(g) and (h), also agree with this behaviour, exhibiting a slight offset in the phase of maximum potential for both waveforms, as compared to the unmagnetised cases. The earlier maximum surface potential indicates an earlier and more rapid sheath collapse, while the sheath expansion, as indicated by the phase of minimum surface potential, occurs at the approximately the same point in phase.

Examining the multi-frequency sheath behaviour in figure 10(d) in more detail, the peak-type driven sheath edge remains approximately static between phases 0.1–0.5 before varying in-sync with the dielectric surface potential. This differs from the unmagnetised case, where the sheath extent follows the surface potential for the full phase cycle. This change arises as the inter-peak portion of the dielectric surface

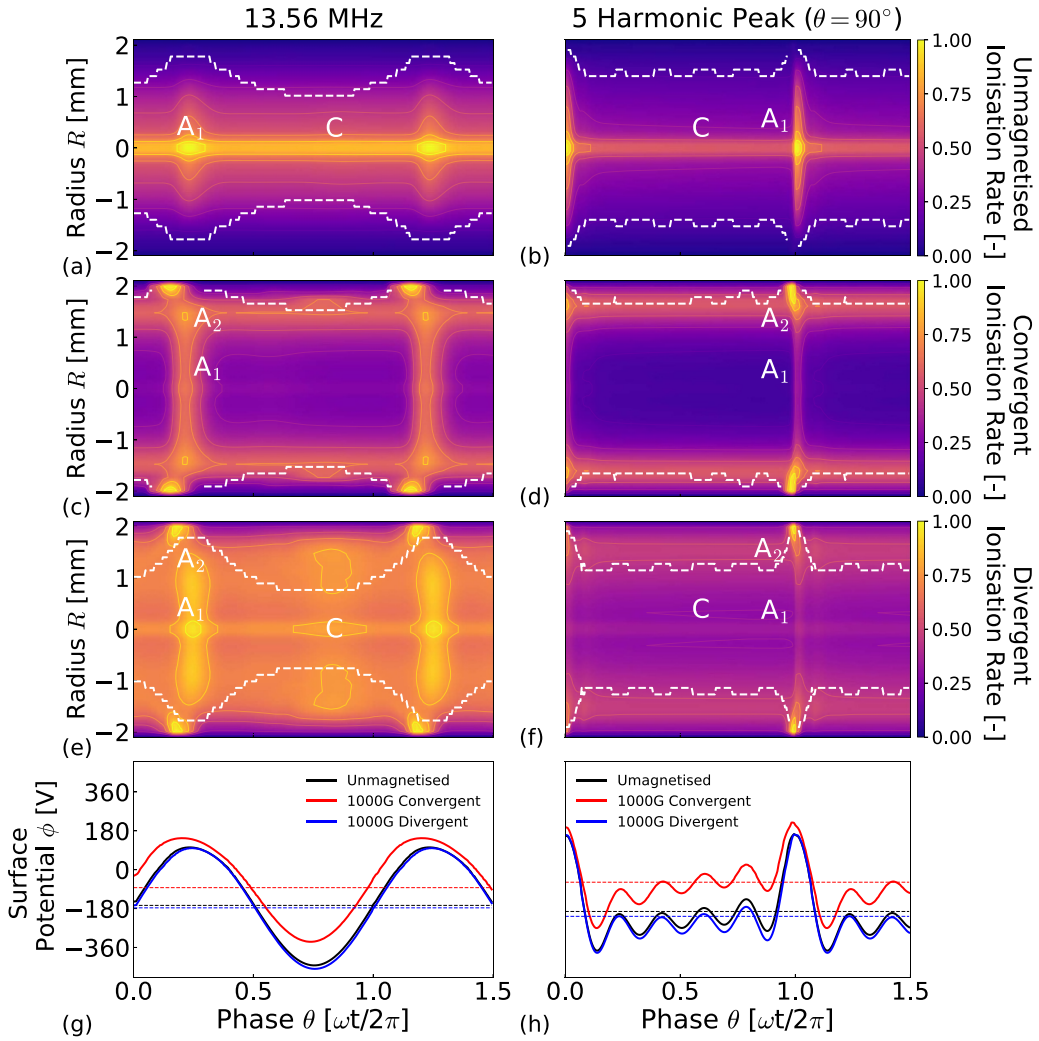

Figure 10. Phase-resolved ionisation rates for single-frequency 13.56 MHz and 'peak'- type tailored voltage waveforms for three magnetic field configurations: unmagnetized, convergent and divergent. The ionisation rates for the single-frequency case are shown in panels (a), (c) and (e) respectively, and those for peak-type waveform case are shown in panels (b), (d) and (f), respectively. The phase-resolved sheath edge is denoted by the white dashed lines in (a)–(f). The corresponding phase-resolved alumina surface potential adjacent to the powered electrode ($R, Z = 2.1$ mm, 21 mm) is presented for (g) 13.56 MHz operation and (h) multi-frequency operation. Dashed lines in (g) and (h) denote the phase-averaged DC self-bias voltage. Operating conditions: plenum pressure 200 pa (1.5 Torr) argon, 600 V_{pp}, magnetic field strengths between $0 \leqslant \mathbf{B} \leqslant 1000$ G.

potential (phases 0.1–0.9) now exhibits an upward gradient, while it was relatively flat between peaks in the unmagnetised case. Normally a more negative surface bias would result in a wider sheath, however, in the magnetised case the sheath cannot extend any further as it is being suppressed by the high secondary electron ionisation at the sheath edge. This demonstrates how the MAE can interact with the mechanisms that underpin the EAE, in this case enforcing a narrower and less dynamic sheath than would otherwise be expected, through enforcing off-axis bulk and secondary ionisation structures.

The sheath and ionisation dynamics for an applied 1000 G divergent magnetic field are presented in figures 10(e) and (f). Here, the behaviour between the single frequency and peak-type waveform driven discharges is quite different to the convergent case. The single frequency discharge in figure 10(e) exhibits predominately on-axis sheath collapse heating, with a smaller secondary sheath localised heating peak, denoted A_1 and A_2, respectively. The re-emergence of the on-axis sheath collapse heating peak arises due to the magnetic minima in-line with the powered electrode (see figure 3(c)) increasing the radial electron transport at this location. Similarly the secondary electron ionisation is also observed back on-axis, peaking immediately following the phase of most negative surface bias. There are also two, off-axis, secondary ionisation structures between phases 0.6–0.9, aligning with the maximum on-axis secondary ionisation rate. These represent secondary ionisations within the sheath due to the reduction in electric field strength, leading to slower secondary electrons with lower mean-free-paths, as the sheath reaches maximum extension.

The multi-frequency peak-type discharge in figure 10(f) exhibits a narrow radially extended sheath collapse ionisation structure, peaking immediately adjacent to the radial wall at $\theta = 1.0$. Secondary ionisation still occurs predominately at high radii, due to the magnetisation of secondary electrons

upstream and downstream of the powered electrode. However, due to the minimised magnetic field adjacent across the source at $Z = 21$ mm, the secondary electron ionisation rate, and hence population, is more evenly distributed across the full radius of the hollow cathode channel. The on-axis ionisation rate is approximately half of the peak off-axis ionisation rate, as compared to a factor of 1000 for the converging topology, where almost all secondary electrons are confined to within a Larmor radius of the sheath edge. In both the single and multi-frequency diverging field cases, the relatively lower magnetised radial electron flux upstream and downstream of the powered electrode necessitates a wider sheath at the powered electrode to inhibit the unmagnetised radial electron flux to the powered electrode and maintain quasineutrality. As the amplitude of the surface bias remains similar for the unmagnetised and diverging magnetised cases, presented in figure 10(h), then the relative phase-resolved variation of the sheath introduced by the EAE is smaller compared to the now wider phase-averaged sheath extent. In effect, the sheath is less dynamic than it would in an unmagnetised case with the same applied voltage waveform.

The significantly different DC self-bias modulations, ionisation structures, and sheath dynamics resulting from the simultaneous application of the EAE and MAE demonstrated in figures 9 and 10 illustrates that the effects of the EAE and MAE cannot be treated in isolation. This differs from the linearly additive DC self-bias modulation observed when the EAE is applied to an unmagnetised physically asymmetric source. Further the topology of the magnetic field, relative to the powered electrode sheath, has a significant effect on the EAE through altering the behaviour of bulk and secondary electrons adjacent to the sheath edge. Therefore, to adequately model magnetised multi-frequency or low-frequency discharges, where sheath dynamics are most important, a fully phase-resolved treatment of the plasma response and secondary electron motion is required. The capability to mediate, enhance, and inhibit the EAE via the MAE provides an additional control variable to fine-tune discharge parameters, such as discharge homogeneity and particle energy distribution functions in CCPs.

5. Conclusions

The MAE has been demonstrated via 2D fluid/kinetic simulations of a non-planar capacitively coupled RF discharge employing both single and multi-frequency voltage waveforms, operated in 1.5 Torr of argon. The MAE was characterised for two magnetic topologies, a converging topology and a diverging topology, where the magnetic field strength on-axis in line with the powered electrode was maximised and minimised, respectively. Application of the MAE alone resulted in an up-modulation in the DC self-bias by $+0.13$ V_{pp} and a down-modulation by -0.03 V_{pp}, as compared to an unmagnetised discharge, for applied 1000 G converging and diverging magnetic topologies, respectively. In both cases, control of the DC self-bias voltage was achieved through varying the net positive and negative fluxes to the powered electrode through selective magnetisation of the electrons. Converging magnetic topologies exhibited an 40% enhanced charged flux to the powered electrode, while diverging magnetic topologies exhibited an 15% reduced charged flux to the powered electrode. The larger effect exhibited by the converging magnetic topology is attributed to a radial confinement of the secondary electron population adjacent to the sheath edge, resulting in significant localised ionisation, and hence higher radial fluxes, and a reduction in the phase-averaged sheath extent.

Simultaneous application of an EAE and MAE was achieved via the application of five-harmonic 'peak'-type tailored voltage waveforms. The EAE was predominately unaffected by the diverging magnetic topology, exhibiting no change to the most positive DC self-bias voltage, and a -0.04 V_{pp} reduction to the most negative DC self-bias voltage, a value that agrees with the reduction achieved by the MAE alone. In contrast the EAE was significantly affected by the application of a converging magnetic topology, exhibiting an averaged $+0.28$ V_{pp} increase in the DC self-bias voltage over the phase-offset range $0^\circ \leqslant \theta \leqslant 360^\circ$. The phase offsets resulting in the minimum and maximum DC self-bias voltages also exhibited a 60° shift. Most notably, the average 0.28 V_{pp} modulation achieved via the simultaneous application of an EAE and converging topology MAE did not equal a linear combination of the 0.23 V_{pp} and 0.13 V_{pp} modulations achieved, respectively, by each effect in isolation. This demonstrates a degree of non-linear coupling between the MAE and EAE, driven primarily via the sheath edge confinement of secondary electrons, which must be taken into account in order to reliably model magnetised multi-frequency RF discharges. Further studies into the non-linearity achieved via the simultaneous application of electric and magnetic control schemes will enable enhanced decoupling and control of the electron and ion dynamics in RF discharges, and represents an improvement over each system in isolation.

Data availability statement

The data that support the findings of this study are openly available upon reasonable request to the corresponding author.

Acknowledgments

The authors gratefully acknowledge Prof. Mark J Kushner and Dr Andrew R Gibson for insightful discussions. This work was supported by the UK Engineering and Physical Sciences Research Council (EPSRC), Grant Reference Number: EP/m508196/1. Data underpinning the figures presented in this work are available upon request.

ORCID iDs

Scott J Doyle https://orcid.org/0000-0002-8741-1018
James P Dedrick https://orcid.org/0000-0003-4353-104X

References

[1] Adamovich I *et al* 2017 The 2017 plasma roadmap: low temperature plasma science and technology *J. Phys. D: Appl. Phys.* **50** 323001
[2] Donkó Z, Derzsi A, Vass M'e, Schulze J, Schuengel E and Hamaguchi S 2018 Ion energy and angular distributions in low-pressure capacitive oxygen RF discharges driven by tailored voltage waveforms *Plasma Sources Sci. Technol.* **27** 104008
[3] Lafleur T and Booth J P 2012 Control of the ion flux and ion energy in CCP discharges using non-sinusoidal voltage waveforms *J. Phys. D: Appl. Phys.* **45** 395203
[4] Bárdoš L 1996 Radio frequency hollow cathodes for the plasma processing technology *Surf. Coat. Technol.* **86–87** 648–56
[5] Doyle S J, Lafleur T, Gibson A R, Tian P, Kushner M J and Dedrick J 2017 Enhanced control of the ionization rate in radio-frequency plasmas with structured electrodes via tailored voltage waveforms *Plasma Sources Sci. Technol.* **26** 125005
[6] Kanarik K J, Lill T, Hudson E A, Sriraman S, Tan S, Marks J, Vahedi V and Gottscho R A 2015 Overview of atomic layer etching in the semiconductor industry *J. Vac. Sci. Technol.* A **33** 020802
[7] Dixon S, Charles C, Boswell R W, Cox W, Holland J and Gottscho R 2013 Interactions between arrayed hollow cathodes *J. Phys. D: Appl. Phys.* **46** 145204
[8] Horwitz C M 1988 Hollow cathode etching and deposition *J. Vac. Sci. Technol.* A **6** 1837
[9] Levchenko I *et al* 2018 Space micropropulsion systems for Cubesats and small satellites: from proximate targets to furthermost frontiers *Appl. Phys. Rev.* **5** 011104
[10] Charles C, Liang W, Raymond L, Rivas-Davila J and Boswell R W 2017 Vacuum testing of a miniaturized switch mode amplifier powering an electrothermal plasma micro-thruster *Front. Phys.* **5** 1–8
[11] Mazouffre S 2016 Electric propulsion for satellites and spacecraft: established technologies and novel approaches *Plasma Sources Sci. Technol.* **25** 033002
[12] Arakoni R A, Ewing J J and Kushner M J 2008 Microdischarges for use as microthrusters: modelling and scaling *J. Phys. D: Appl. Phys.* **41** 105208
[13] Lazzaroni C, Chabert P, Rousseau A and Sadeghi N 2010 Sheath and electron density dynamics in the normal and self-pulsing regime of a micro hollow cathode discharge in argon gas *Eur. Phys. J.* D **60** 555–63
[14] Schulze J, Heil B G, Luggenhölscher D, Brinkmann R P, Czarnetzki U and Luggenh D 2008 Stochastic heating in asymmetric capacitively coupled RF discharges *J. Phys. D: Appl. Phys.* **41** 195212
[15] Lafleur T and Chabert P 2015 Is collisionless heating in capacitively coupled plasmas really collisionless? *Plasma Sources Sci. Technol.* **24** 044002
[16] Perret A, Chabert P, Jolly J and Booth J-P 2005 Ion energy uniformity in high-frequency capacitive discharges *Appl. Phys. Lett.* **86** 10–13
[17] O'Connell D, Zorat R, Ellingboe A R and Turner M M 2007 Comparison of measurements and particle-in-cell simulations of ion energy distribution functions in a capacitively coupled radio-frequency discharge *Phys. Plasmas* **14** 103510
[18] Liu J, Huppert G L and Sawin H H 1990 Ion bombardment in rf plasmas *J. Appl. Phys.* **68** 3916–34
[19] Schoenbach K H, El-habachi A, Shi W and Ciocca M 1997 High-pressure hollow cathode discharges *Plasma Sources Sci. Technol.* **6** 468–77
[20] Lafleur T and Boswell R W 2012 Particle-in-cell simulations of hollow cathode enhanced capacitively coupled radio frequency discharges *Phys. Plasmas* **19** 023508
[21] Doyle S J, Gibson A R, Flatt J, Ho T S, Boswell R W, Charles C, Tian P, Kushner M J and Dedrick J 2018 Spatio-temporal plasma heating mechanisms in a radio-frequency electrothermal microthruster *Plasma Sources Sci. Technol.* **27** 085011
[22] Schulze J, Schüngel E, Donkó Z and Czarnetzki U 2010 Charge dynamics in capacitively coupled radio frequency discharges *J. Phys. D: Appl. Phys.* **43** 225201
[23] Lieberman M A 1988 Analytical solution for capacitive RF sheath *IEEE Trans. Plasma Sci.* **16** 638–44
[24] Ho T S 2018 Supersonic constricted plasma flows *PhD Thesis* Australian National University
[25] Schmidt N, Schulze J, Schüngel E and Czarnetzki U 2013 Effect of structured electrodes on heating and plasma uniformity in capacitive discharges *J. Phys. D: Appl. Phys.* **46** 505202
[26] Lieberman M A and Lichtenberg A J 2005 *Principles of Plasma Discharges and Materials Processing* 2nd edn (Wiley)
[27] Korolov I, Derzi A, Donkó Z, Schüngel E and Schulze J 2016 The influence of electron reflection / sticking coefficients at the electrodes on plasma parameters in particle-in-cell simulations of capacitive radio-frequency plasmas *Plasma Sources Sci. Technol.* **25** 015024
[28] Lafleur T, Chabert P and Booth J P 2013 Secondary electron induced asymmetry in capacitively coupled plasmas *J. Phys. D: Appl. Phys.* **46** 135201
[29] Derzsi A, Korolov I, Schüngel E, Donkó Z and Schulze J 2015 Effects of fast atoms and energy-dependent secondary electron emission yields in PIC/MCC simulations of capacitively coupled plasmas *Plasma Sources Sci. Technol.* **24** 034002
[30] Horváth B, Derzsi A, Schulze J, Korolov I, Hartmann P and Donkó Z 2020 Experimental and kinetic simulation study of electron power absorption mode transitions in capacitive radiofrequency discharges in neon *Plasma Sources Sci. Technol.* **29** 055002
[31] Schüngel E, Mohr S, Schulze J, Czarnetzki U and Kushner M J 2013 Ion distribution functions at the electrodes of capacitively coupled high-pressure hydrogen discharges *Plasma Sources Sci. Technol.* **23** 015001
[32] Doyle S J, Gibson A R, Boswell R W, Charles C and Dedrick J P 2019 Inducing locally structured ion energy distributions in intermediate-pressure plasmas Inducing locally structured ion energy distributions in intermediate-pressure plasmas *Phys. Plasmas* **7** 073519
[33] Ries S, Banko L, Hans M, Primetzhofer D, Schneider J M, Ludwig A, Awakowicz P and Schulze J 2019 Ion energy control via the electrical asymmetry effect to tune coating properties in reactive radio frequency sputtering *Plasma Sources Sci. Technol.* **28** 114001
[34] Goto H H, Sasaki M, Ohmi T, Shibata T, Yamagami A, Okamura N and Kamiya O 1990 Related content minimizing wafer surface damage and chamber material contamination in new plasma processing equipment *Jpn. J. Appl. Phys.* **29** 2395–7

[35] Day M E, Delfino M and Salimian S 1992 Low energy ion etching of aluminum oxide films and native aluminum oxide *J. Appl. Phys.* **72** 5467–70
[36] Heil B G, Czarnetzki U, Brinkmann R P and Mussenbrock T 2008 On the possibility of making a geometrically symmetric RF-CCP discharge electrically asymmetric *J. Phys. D: Appl. Phys.* **41** 165202
[37] Schulze J, Schüngel E, Czarnetzki U and Donko Z 2009 Optimization of the electrical asymmetry effect in dual-frequency capacitively coupled radio frequency discharges: experiment, simulation and model *J. Appl. Phys.* **106** 092005
[38] Schüngel E, Eremin D, Schulze J, Mussenbrock T and Czarnetzki U 2012 The electrical asymmetry effect in geometrically asymmetric capacitive radio frequency plasmas *J. Appl. Phys.* **112** 053302
[39] Lafleur T, Chabert P, Turner M M and Booth J P 2013 Theory for the self-bias formation in capacitively coupled plasmas excited by arbitrary waveforms *Plasma Sources Sci. Technol.* **22** 065013
[40] Turner M M and Chabert P 2014 A radio-frequency sheath model for complex waveforms *Appl. Phys. Lett.* **104** 0–4
[41] Gibson A R *et al* 2019 Disrupting the spatio-temporal symmetry of the electron dynamics in atmospheric pressure plasmas by voltage waveform tailoring *Plasma Sources Sci. Technol.* **28** 01LT01
[42] Doyle S J, Gibson A R, Boswell R W, Charles C and Dedrick J P 2019 Control of electron, ion and neutral heating in a radio-frequency electrothermal microthruster via dual-frequency voltage waveforms *Plasma Sources Sci. Technol.* **28** 035019
[43] Gans T, Schulze J, O'Connell D, Czarnetzki U, Faulkner R, Ellingboe A R and Turner M M 2006 Frequency coupling in dual frequency capacitively coupled radio-frequency plasmas *Appl. Phys. Lett.* **89** 13–16
[44] Oberberg M, Engel D, Berger B, Wölfel C, Eremin D, Lunze J, Brinkmann R P, Awakowicz P and Schulze J 2019 Magnetic control of nonlinear electron resonance heating in a capacitively coupled radio frequency discharge *Plasma Sources Sci. Technol.* **28** 115021
[45] Oberberg M, Kallahn J, Awakowicz P and Schulze J 2018 Experimental investigations of the magnetic asymmetry effect in capacitively coupled radio frequency plasmas *Plasma Sources Sci. Technol.* **27** 105018
[46] Kushner M J 2003 Modeling of magnetically enhanced capacitively coupled plasma sources: Ar discharges *J. Appl. Phys.* **94** 1436
[47] Yang S, Zhang Y, Wang H, Cui J and Jiang W 2017 Magnetical asymmetric effect in geometrically and electrically symmetric capacitively coupled plasma *Plasma Process. Polym.* **14** 1–9
[48] Yang S, Chang L, Zhang Y and Jiang W 2018 Magnetical asymmetry effect in capacitively coupled plasmas: effects of the magnetic field gradient, pressure and gap length *Plasma Sources Sci. Technol.* **27** 035008
[49] Sharma S, Mishra S K, Kaw P K, Das A, Sirse N and Turner M M 2015 Collisionless sheath heating in current-driven capacitively coupled plasma discharges via higher order sinusoidal signals *Plasma Sources Sci. Technol.* **24** 025037
[50] Charles C and Boswell R W 2012 Measurement and modelling of a radiofrequency micro-thruster *Plasma Sources Sci. Technol.* **21** 022002
[51] Charles C, Dedrick J, Boswell R W, O'Connell D and Gans T 2013 Nanosecond optical imaging spectroscopy of an electrothermal radiofrequency plasma thruster plume *Appl. Phys. Lett.* **103** 124103
[52] Greig A, Charles C, Paulin N and Boswell R W 2014 Volume and surface propellant heating in an electrothermal radio-frequency plasma micro-thruster *Appl. Phys. Lett.* **105** 054102
[53] Greig A, Charles C and Boswell R W 2015 Simulation of main plasma parameters of a cylindrical asymmetric capacitively coupled plasma micro-thruster using computational fluid dynamics *Front. Phys.* **2** 1–9
[54] Ho T S, Charles C and Boswell R W 2017 A comprehensive cold gas performance study of the pocket rocket radiofrequency electrothermal microthruster *Front. Phys.* **4** 1–16
[55] Ho T S, Charles C and Boswell R 2017 Neutral gas heating and ion transport in a constricted plasma flow *Phys. Plasmas* **24** 8–13
[56] Ho T S, Charles C and Boswell R W 2018 Performance modelling of plasma microthruster nozzles in vacuum *J. Appl. Phys.* **123** 173301
[57] Kushner M J 2009 Hybrid modelling of low temperature plasmas for fundamental investigations and equipment design *J. Phys. D: Appl. Phys.* **42** 194013
[58] Scharfetter D L and Gummel H K 1969 Large-signal analysis of a silicon read diode oscillator *IEEE Trans. Electron Devices* **16** 64–77
[59] Agarwal A, Rauf S and Collins K 2012 Gas heating mechanisms in capacitively coupled plasmas *Plasma Sources Sci. Technol.* **21** 055012
[60] Charles C, Hawkins R and Boswell R W 2015 Particle in cell simulation of a radiofrequency plasma jet expanding in vacuum *Appl. Phys. Lett.* **106** 093502
[61] Tian P and Kushner M J 2015 Controlling VUV photon fluxes in low-pressure inductively coupled plasmas *Plasma Sources Sci. Technol.* **24** 034017
[62] Hayashi M yr1991 *Technical Report* IPPJ-AM-19 Nagoya Institute of Technology
[63] Tachibana K 1986 Excitation of the $1s_5$, $1s_4$, $1s_3$ and $1s_2$ levels of argon by low-energy electrons *Phys. Rev.* A **34** 451
[64] Rapp D and Englander Golden P 1965 Total cross sections for ionization and attachment in gases by electron impact. I. Positive ionization *J. Chem. Phys.* **43** 1464–79
[65] Dyatko N A, Ionikh Y Z, Kochetov I V, Marinov D L, Meshchanov A V, Napartovich A P, Petrov F B and Starostin S A 2008 Experimental and theoretical study of the transition between diffuse and contracted *J. Phys. D: Appl. Phys* **41** 055204
[66] Bogaerts A, Serikov R G V and Serikov V V 1999 Calculation of gas heating in direct current argon glow discharges *J. Appl. Phys.* **87** 8334
[67] Ellis H W, Pai R Y, McDaniel E W, Mason E A and Viehland L A 1976 Transport properties of gaseous ions over a wide energy range *At. Data Nucl. Data tables* **17** 177–210
[68] Salabaş A and Brinkmann R P 2006 Non-neutral/quasi-neutral plasma edge definition for discharge models: a numerical example for dual frequency hydrogen capacitively coupled plasmas *Japan. J. Appl. Phys.* 1 **45** 5203–6
[69] Lafleur T 2016 Tailored-waveform excitation of capacitively coupled plasmas and the electrical asymmetry effect *Plasma Sources Sci. Technol.* **25** 013001
[70] Zhang Q-Z, Jiang W, Zhao S-X and Wang Y-N 2010 Surface-charging effect of capacitively coupled plasmas driven by combined dc/rf sources *J. Vac. Sci. Technol.* A **28** 287–92
[71] Trieschmann J, Shihab M, Szeremley D, Elfattah Elgendy A, Gallian S, Eremin D, Peter Brinkmann R and Mussenbrock T 2013 Ion energy distribution functions

behind the sheaths of magnetized and non-magnetized radio frequency discharges *J. Phys. D: Appl. Phys.* **46** 084016

[72] Oberberg M, Berger B, Buschheuer M, Engel D, Wölfel C, Eremin D, Lunze J, Brinkmann R P, Awakowicz P and Schulze J 2020 The magnetic asymmetry effect in geometrically asymmetric capacitively coupled radio frequency discharges operated in Ar/O_2 *Plasma Sources Sci. Technol.* **29** 075013

[73] Eremin D *et al* 2023 Electron dynamics in planar radio frequency magnetron plasmas: I. The mechanism of hall heating and the μ-mode *Plasma Sources Sci. Technol.* **32** 045007

[74] James Doyle S, Robert Gibson A, Boswell R W, Charles C and Peter Dedrick J 2020 Decoupling ion energy and flux in intermediate pressure capacitively coupled plasmas via tailored voltage waveforms *Plasma Sources Sci. Technol.* **29** 095018